



Full length article

Structural health monitoring of shell structures with preexisting cracks

Ihtisham Khalid ^a, Zahid Ahmed Qureshi ^a, Yasir Ali ^a, Selda Oterkus ^b,
Erkan Oterkus ^b,*

^a Department of Aerospace Engineering, College of Aeronautical Engineering, National University of Sciences & Technology, Islamabad, Pakistan

^b Department of Naval Architecture, Ocean & Marine Engineering, University of Strathclyde, Glasgow, G4 0LZ, Scotland, United Kingdom

ARTICLE INFO

Communicated by S. Fassois

Keywords:

Structural health monitoring
Plate and shell structures
Stress intensity factor
Shape sensing
Crack tip
iFEM

ABSTRACT

Plate and shell-like structures are widely used in the aerospace, marine, and renewable energy sectors. However, they are susceptible to various defects, especially cracks, during their operational lifespan. Although the inverse Finite Element Method (iFEM) offers significant advantages, such as real-time shape sensing capabilities, its current formulations cannot reconstruct crack mechanics and analyze structures with preexisting cracks. Geometric discontinuities, such as cracks, present unique challenges that require special treatment in fracture mechanics. This study presents a novel inverse crack tip shell element for real-time reconstruction of full-field displacement profiles and computation of Stress Intensity Factors (SIFs), addressing the limitations of current iFEM formulations. The proposed six-node triangular inverse element is flexible in mapping complex geometries and inherently ensures strain singularity at the crack tip by repositioning its mid-side nodes. The proposed inverse formulation is numerically validated against benchmark analytical and high-fidelity Finite Element Method (FEM) reference solutions for varying geometries and crack configurations subjected to different loading and boundary conditions. The study also introduces a variational technique for optimizing sensor locations within the inverse element domain to accurately compute Stress Intensity Factors (SIFs). The proposed inverse shell formulation is computationally efficient and seamlessly integrates within the iFEM framework for real-time shape sensing and Structural Health Monitoring (SHM) of shell structures with preexisting cracks.

1. Introduction

Structural Health Monitoring (SHM) is an essential interdisciplinary technique that continually observes and analyzes structural systems to detect changes in their behavior. The primary objective of any Structural Health Monitoring (SHM) system is to enhance both man and machine safety while simultaneously reducing maintenance costs. Employment of the SHM system involves a periodic collection of sensory data, such as strain measurements, to realize the current state of the engineering structure and to execute a prognosis of its future condition [1]. This prediction involves estimating the remaining useful life of a structure or identifying potential failure modes. The most challenging and pivotal aspect of a robust SHM system is its ability to access real-time structural integrity. Engineering structures are evaluated using various numerical techniques, such as finite element methods [2,3], semi-analytical methods [4,5], variational techniques [6], and more recently, peridynamics [7,8]. Assessment of structural integrity necessitates reconstructing the full-field displacement and stress profiles from onboard sensor data. For example, in the aerospace

* Corresponding author.

E-mail address: erkan.oterkus@strath.ac.uk (E. Oterkus).

<https://doi.org/10.1016/j.ymssp.2025.112663>

Received 17 August 2024; Received in revised form 24 February 2025; Accepted 27 March 2025

Available online 8 April 2025

0888-3270/© 2025 The Authors. Published by Elsevier Ltd. This is an open access article under the CC BY-NC-ND license (<http://creativecommons.org/licenses/by-nc-nd/4.0/>).

or naval sectors, this involves real-time analysis of the vehicle structure to detect any potential integrity issues during operation. Therefore, shape sensing capability is crucial to SHM applications, which poses an inverse problem that has intrigued researchers for their significant contribution to the literature.

Early research in shape sensing focused on applying Ko's Displacement Theory [9] to reconstruct displacement profiles for beam structures. Specifically, Ko et al. [10] utilized the assumptions of Euler–Bernoulli beam theory to reconstruct aircraft wing deflection by strategically placing strain sensors along spar lines on the wing stations. Additional studies [11,12] have explored global and piecewise continuous basis functions for displacement reconstruction. Modal Transformation Theory (MTT) [13,14] has garnered significant attention for its ability to reconstruct displacement profiles from normal mode shapes using appropriate strain–displacement relations. Shkarayev et al. [15] proposed a two-step least squares method for displacement reconstruction, which involves first reconstructing the applied loading on the structure and, subsequently, the displacement field.

More recent advancements have seen the employment of variational approaches to develop full-field shape sensing capabilities using numerical techniques based on the Finite Element Method (FEM). The framework, introduced by Tessler and Spangler [16], formulates a variational error functional using experimental strain data and FEM approximations to reconstruct displacement and stress profiles, thereby enabling real-time shape sensing capabilities during inverse analysis. Based on this framework, the inverse Finite Element Method (iFEM) has emerged as a powerful tool for shape sensing in SHM applications. It offers the potential for real-time damage assessment of various engineering structures.

Developing inverse elements tailored to specific structural configurations demonstrates the versatility of iFEM in ongoing SHM advancements. Tessler et al. [17] presented the first three-node inverse element (iMIN3) for shape sensing applications in plate and shell structures. Kefal et al. [18,19] developed quadrilateral inverse shell elements (iQS4, iCS8) for shape sensing of marine and offshore structures. Recently, Khalid et al. presented inverse plate and shell elements (iKP4, iKS3, and iKS4) to efficiently undertake the shape sensing, structural health monitoring, and damage assessment of thin plate and shell structures [20–22]. De Mooij et al. [23] formulated a twenty-node solid inverse element for the three-dimensional analysis of thick structures. The development of the i3-RZT inverse element [24], based on the Refined Zigzag Theory, has expanded the shape sensing capabilities of iFEM in layered structures, such as composite laminates and sandwich panels. Recently, iFEM has been studied by combining it with physics and statistical-based techniques to improve its full-field prediction capabilities [25,26].

The iFEM framework offers significant advantages from a structural health assessment and damage identification perspective. This framework has enabled precise detection, location, and quantification of localized defects in various structural configurations [27,28]. Researchers have also employed iFEM methodology in combination with the power of Convolutional Neural Networks (CNN) and adaptive baseline modeling to enhance the defect characterization capabilities of iFEM [29,30]. Similarly, Data-driven approaches based on Machine Learning (ML) techniques also provide advantages in predicting structural behavior through advanced pattern recognition techniques [31–33]. Furthermore, probabilistic active learning frameworks [34,35] present an innovative approach to SHM by continuously updating the learning process with real-time data acquisition and analysis. As a result, these approaches present valuable alternatives for various practical SHM applications.

Analysis of cracks under various loading conditions is a critical area of research in understanding failure mechanisms and improving material performance. In literature, researchers have used the phase-field approach to effectively simulate the initiation and propagation of cracks in materials subjected to various loading conditions [36,37]. This approach models cracks as a continuous field, eliminating the need for explicit crack surface tracking and enabling seamless simulation of complex crack patterns [38,39]. By incorporating energy-based criteria, phase-field models accurately predict static and evolving cracks, capturing critical phenomena such as crack branching, deflection, and interactions with material heterogeneities [40,41].

A comprehensive literature review reveals that the effectiveness of iFEM analysis depends significantly on the underlying mechanics incorporated within the inverse formulation. Although numerous inverse elements are available for shape sensing and SHM applications, traditional inverse elements are inadequate for predicting the structural integrity of plate and shell structures with preexisting cracks. These elements cannot accurately capture the required strain singularity at the crack tip. Furthermore, the accurate computation of fracture parameters, such as the stress intensity factor (SIF), critically depends on the optimal placement of sensors around the crack tip. This aspect of sensor optimization has yet to be thoroughly explored in the existing literature for the health assessment of engineering structures with preexisting cracks.

Building on advancements in iFEM, this study introduces a new six-node triangular inverse crack-tip element (hereafter referred to as iTS6). This element extends iFEM capabilities in fracture mechanics and addresses the existing gap in evaluating the structural integrity of plate and shell structures with preexisting cracks. The iTS6 triangular inverse element enables native mapping to the crack tip, unlike quadrilateral elements necessitating degeneration, to ensure strain singularity by repositioning its mid-side nodes. Triangular elements also provide superior flexibility for meshing complex geometries, particularly around irregular boundaries and crack tips, as compared to quadrilateral elements. The isoparametric inverse formulation of the iTS6 element is based on the kinematics of First-Order Shear Deformation Theory (FSDT). Formulations based on FSDT are often prone to induced mechanisms and locking issues. Therefore, the proposed inverse formulation employs an assumed linear shear strain field and a full Gauss integration scheme to mitigate these issues. The iTS6 inverse element seamlessly integrates with the iFEM existing framework, ensuring compatibility for shape sensing in both cracked and uncracked structures. A detailed numerical validation study demonstrates the effectiveness of the proposed formulation in full-field reconstruction of displacement profiles and key fracture parameters, i.e., Stress Intensity Factors (SIFs). The study also presents a variational methodology to optimize sensor placement around the cracks to maximize strain measurement precision and enhance the reliability of fracture parameter computations in SHM applications.

The rest of the article is structured as follows: The inverse element formulation is presented systematically, along with theoretical insights into finite element approximation, strain singularity, and the formulation of the iFEM weighted least squares functional. These insights are paramount to understanding the proposed formulation and its influence on iFEM analysis and interpretation of results. The numerical validation section evaluates the proposed inverse formulation against analytical and high-fidelity FEM reference solutions. This section demonstrates the practicality and effectiveness of the iTS6 inverse element in shape sensing and predicting key fracture parameters in real-world scenarios. A least squares variational study is also conducted in the numerical validation section to optimize sensor placement in structures with preexisting cracks. Finally, the conclusion section highlights the significant findings and the effectiveness of the proposed inverse element for real-time health assessment of engineering structures with preexisting cracks.

2. Inverse element formulation

Plate theories are essential for the theoretical and numerical analysis of two-dimensional plate and shell structures. Classical Plate Theory (CPT) simplifies the analysis of thin plate problems with reasonable accuracy, but in practical applications, such as FEM, the C^1 continuity requirements of CPT make it challenging to achieve a conforming displacement field. Reissner and Mindlin addressed this complexity by relaxing one of CPT's assumptions, allowing for transverse shear deformation effects analogous to Timoshenko beam theory. Their formulation assumes that normal material lines are not necessarily orthogonal to the mid-plane after deformation. First-order shear Deformation Theory (FSDT) extends these principles, providing a more accurate representation of shear strains through the plate thickness, often by incorporating a shear correction factor. The kinematics of FSDT are less stringent and versatile enough to undertake practical applications, i.e., FEM and iFEM, of thin and moderately thick plates made of homogeneous and composite materials.

2.1. Displacement field

The displacement field (\mathbf{u}) of a three-dimensional plate, according to the FSDT assumptions, can be expressed as:

$$u(x, y, z) = u_o(x, y) - z\theta_x(x, y) \quad (1a)$$

$$v(x, y, z) = v_o(x, y) - z\theta_y(x, y) \quad (1b)$$

$$w(x, y, z) = w_o(x, y) \quad (1c)$$

In these equations, the subscript o indicates that the displacements are evaluated at the mid-plane of the plate at $z = 0$. The variables u_o and v_o correspond to in-plane displacements along the longitudinal and lateral directions of the plate, while w_o represents the out-of-plane deflection. Alongside the transverse deflection, the angles θ_x and θ_y indicate rotations of the plate normal around the y and x axes, respectively.

Inclusion of the independent rotations (θ_x, θ_y) in the kinematic assumptions of FSDT enhances its ability to reconstruct displacement field under various physical conditions. These conditions include localized deformation effects caused by concentrated loads, which significantly influence strain distribution, and scenarios where transverse shear and bending interactions dominate, such as boundary-layer effects in moderately thick plates subjected to complex constraints.

2.2. Strain field

The strain–displacement relations for the FSDT are derived from the displacement field in Eq. (1) using the theory of elasticity and the assumption of compatibility of strains. If we neglect insignificant strain components in the strain field, the strain displacement relations can be expressed as follows:

$$\varepsilon_{xx} = \frac{\partial u_o}{\partial x} - z \frac{\partial \theta_x}{\partial x} \quad (2a)$$

$$\varepsilon_{yy} = \frac{\partial v_o}{\partial y} - z \frac{\partial \theta_y}{\partial y} \quad (2b)$$

$$\gamma_{xy} = \frac{\partial u_o}{\partial y} + \frac{\partial v_o}{\partial x} - z \left(\frac{\partial \theta_x}{\partial y} + \frac{\partial \theta_y}{\partial x} \right) \quad (2c)$$

$$\gamma_{xz} = \frac{\partial w_o}{\partial x} - \theta_x \quad (2d)$$

$$\gamma_{yz} = \frac{\partial w_o}{\partial y} - \theta_y \quad (2e)$$

In FSDT, the strain field includes all components of in-plane strains; two normal strains ($\varepsilon_{xx}, \varepsilon_{yy}$) and a shear strain (γ_{xy}). However, in the transverse direction, the normal transverse strain vanishes owing to general plate assumptions ($\varepsilon_{zz} = 0$), and transverse shear strains (γ_{xz}, γ_{yz}) are constant throughout the thickness.

The strain field in Eq. (2) can be rewritten more conveniently by segregating the membrane, bending, and shear components separately.

$$\boldsymbol{\varepsilon}^o(\mathbf{u}) = \begin{Bmatrix} \varepsilon_{xx}^o \\ \varepsilon_{yy}^o \\ \gamma_{xy}^o \end{Bmatrix} = \begin{Bmatrix} \frac{\partial u_o}{\partial x} \\ \frac{\partial v_o}{\partial y} \\ \frac{\partial u_o}{\partial y} + \frac{\partial v_o}{\partial x} \end{Bmatrix} \quad (3)$$

where $\boldsymbol{\varepsilon}^o(\mathbf{u})$ represents the in-plane components of the membrane strains. These strains are derived from the displacement field in the x and y directions.

$$\boldsymbol{\varepsilon}^k(\mathbf{u}) = \begin{Bmatrix} \varepsilon_{xx}^k \\ \varepsilon_{yy}^k \\ \varepsilon_{xy}^k \end{Bmatrix} = - \begin{Bmatrix} \frac{\partial \theta_x}{\partial x} \\ \frac{\partial \theta_y}{\partial y} \\ \frac{\partial \theta_x}{\partial y} + \frac{\partial \theta_y}{\partial x} \end{Bmatrix} \quad (4)$$

$\boldsymbol{\varepsilon}^k(\mathbf{u})$ comprises the bending strains associated with bending curvatures. These are derived from the rotations about y and x axis, respectively.

$$\boldsymbol{\gamma}^o(\mathbf{u}) = \begin{Bmatrix} \gamma_{xz}^o \\ \gamma_{yz}^o \end{Bmatrix} = \begin{Bmatrix} \frac{\partial w_o}{\partial x} - \theta_x \\ \frac{\partial w_o}{\partial y} - \theta_y \end{Bmatrix} \quad (5)$$

Likewise, the transverse shear strain components are represented as $\boldsymbol{\gamma}^o(\mathbf{u})$. These strains account for the out-of-plane deformations and rotations. In a more compact form, the strain field can be expressed as:

$$\boldsymbol{\varepsilon}(\mathbf{u}) = \begin{Bmatrix} \varepsilon_{xx}^o \\ \varepsilon_{yy}^o \\ \gamma_{yz}^o \\ \gamma_{xz}^o \\ \gamma_{xy}^o \end{Bmatrix} + z \begin{Bmatrix} \varepsilon_{xx}^k \\ \varepsilon_{yy}^k \\ \gamma_{yz}^k \\ \gamma_{xz}^k \\ \gamma_{xy}^k \end{Bmatrix} = \begin{Bmatrix} \boldsymbol{\varepsilon}^o(\mathbf{u}) \\ \boldsymbol{\gamma}^o(\mathbf{u}) \end{Bmatrix} + z \begin{Bmatrix} \boldsymbol{\varepsilon}^k(\mathbf{u}) \\ 0 \end{Bmatrix} \quad (6)$$

Here, $\boldsymbol{\varepsilon}(\mathbf{u})$ represents the strain field, which is the sum of the membrane strains $\boldsymbol{\varepsilon}^o(\mathbf{u})$ and the bending strains $\boldsymbol{\varepsilon}^k(\mathbf{u})$, scaled by the distance from the mid-plane z . The transverse shear strains $\boldsymbol{\gamma}^o(\mathbf{u})$ are included directly, while their bending counterparts are assumed to be zero.

2.3. Stress-strain relations

Within the framework of FSDT, the constitutive relationship between non-zero stress and strain states can be established for a material exhibiting homogeneity and subjected to isothermal conditions.

$$\boldsymbol{\sigma}(\mathbf{u}) = \mathbf{D}\boldsymbol{\varepsilon}(\mathbf{u}) \quad (7)$$

where \mathbf{D} is the constitutive matrix containing the material properties. Due to the plate theory assumptions, the normal stress in the thickness direction ($\sigma_{zz} = 0$) is zero. By substituting the previously derived expressions for membrane, bending, and shear strains into Eq. (7), we can obtain the stress field as:

$$\boldsymbol{\sigma}(\mathbf{u}) = \begin{bmatrix} \mathbf{D}_1 & \vdots & 0 \\ \dots & \vdots & \dots \\ 0 & \vdots & \mathbf{D}_2 \end{bmatrix} \left(\begin{Bmatrix} \boldsymbol{\varepsilon}^o(\mathbf{u}) \\ \boldsymbol{\gamma}^o(\mathbf{u}) \end{Bmatrix} + z \begin{Bmatrix} \boldsymbol{\varepsilon}^k(\mathbf{u}) \\ 0 \end{Bmatrix} \right) \quad (8)$$

The constitutive matrices \mathbf{D}_1 and \mathbf{D}_2 for an orthotropic material can be expressed as follows:

$$\mathbf{D}_1 = \frac{1}{1 - \nu_{12}\nu_{21}} \begin{bmatrix} E_1 & \nu_{21}E_1 & 0 \\ \nu_{12}E_1 & E_2 & 0 \\ 0 & 0 & (1 - \nu_{12}\nu_{21})G_{12} \end{bmatrix}$$

$$\mathbf{D}_2 = \begin{bmatrix} s_{11}G_{13} & 0 \\ 0 & s_{22}G_{23} \end{bmatrix}$$

where E , ν , and G represent Young's modulus, Poisson's ratio, and Shear modulus of elasticity. In FSDT, s_{ij} signifies the shear correction parameters used to calculate the transverse shear stress components.

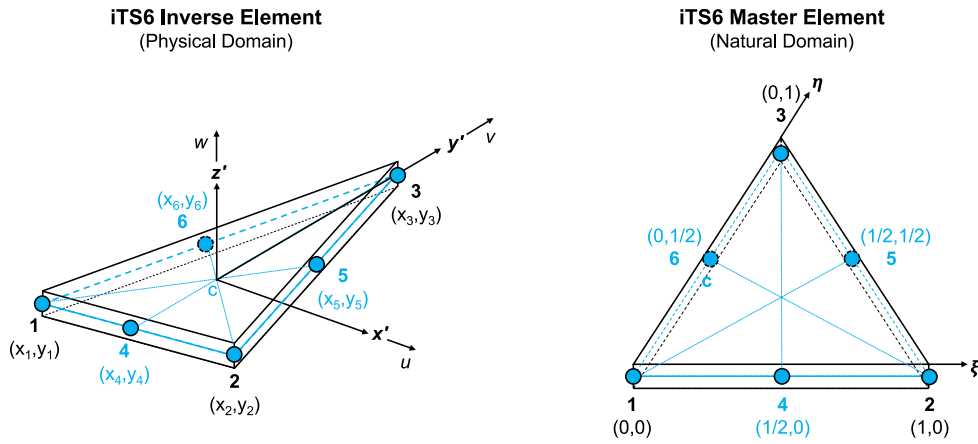


Fig. 1. iTS6 element defined in the physical and natural coordinate system.

2.4. Finite element approximation

A six-node triangular element considered for the finite element approximation is defined in the physical coordinate system with all nodes located at the mid-plane, i.e., $z \in [-t/2, t/2]$, where t represents the thickness of the element, as shown in Fig. 1. A corresponding master element is defined in the triangular natural coordinate system (ξ, η) with all nodes positioned at the mid-plane.

Quadratic basis functions are used to interpolate geometrical domains and generalized displacements for a six-node triangular element. These quadratic basis functions $N_i(\xi, \eta)$ maintain compatibility with linear interpolation along the edges of the triangle.

$$N(\xi, \eta) = \sum_{i=1}^6 N_i(\xi, \eta) \quad (i = 1, 2, \dots, 6) \tag{9}$$

Explicitly, for each node of the triangular element, the basis functions are defined as follows.

$$\begin{aligned} N_1 &= \xi(2\xi - 1) & N_2 &= \eta(2\eta - 1) & N_3 &= \zeta(2\zeta - 1) \\ N_4 &= 4\xi\eta & N_5 &= 4\eta\zeta & N_6 &= 4\xi\zeta \end{aligned}$$

where, $\zeta = (1 - \xi - \eta)$ in the area barycentric coordinates of a triangular element $\xi, \eta, \zeta \in [0, 1]$.

Based on the displacement field given in Eq. (1) and assumptions of FSDT, the nodal displacement vector is represented by five DOFs for the iTS6 inverse element.

$$\mathbf{u}_i^e = \begin{Bmatrix} (u_o)_i \\ (v_o)_i \\ (w_o)_i \\ (\theta_x)_i \\ (\theta_y)_i \end{Bmatrix} \quad (i = 1, 2, \dots, 6) \tag{10}$$

For the i th node of inverse element, (u_o, v_o, w_o) are the nodal displacements, and (θ_x, θ_y) are the bending rotations along the y and x axis, respectively. During iFEM analysis, these unknown nodal displacements are computed and then interpolated over the entire elemental domain Ω^{el} to accomplish displacement distribution over the entire element. Following the conventional finite element methodology, the strain gradient matrices for the iTS6 inverse element are formulated using membrane, bending, and shear strain components.

The in-plane translational displacement variables u_o and v_o in Eq. (1) can be independently interpolated in terms of nodal displacements u and v using quadratic basis functions expressed in Eq. (9).

$$u = \sum_{i=1}^6 N_i(\xi, \eta) (u_o)_i \tag{11}$$

$$v = \sum_{i=1}^6 N_i(\xi, \eta) (v_o)_i \tag{12}$$

Then, the element membrane strains $\epsilon^o(\mathbf{u}^e)$ can be computed using Eqs. (11) and (12) in Eq. (3).

$$\epsilon^o(\mathbf{u}^e) = \mathbf{B}^m \mathbf{u}^e \tag{13}$$

where \mathbf{B}^m represents the element membrane gradient matrix, which can be written as follows for the i th node.

$$\mathbf{B}_i^m = \begin{bmatrix} \frac{\partial N_i}{\partial x} & 0 & 0 & 0 & 0 \\ 0 & \frac{\partial N_i}{\partial y} & 0 & 0 & 0 \\ \frac{\partial N_i}{\partial y} & \frac{\partial N_i}{\partial x} & 0 & 0 & 0 \end{bmatrix} \quad (i = 1, 2, \dots, 6) \quad (14)$$

The complete element membrane gradient matrix can now be populated by substituting \mathbf{B}_i^m for all element nodes ($i = 1, 2, 3, \dots, 6$).

$$\mathbf{B}^m = [\mathbf{B}_1^m \quad \mathbf{B}_2^m \quad \mathbf{B}_3^m \quad \mathbf{B}_4^m \quad \mathbf{B}_5^m \quad \mathbf{B}_6^m] \quad (15)$$

In contrast to CPT, the bending variables of FSDT necessitates C^0 continuity at the element edges; therefore, the bending rotations can be defined using the same basis functions presented in Eq. (9).

$$\theta_x = \sum_{i=1}^6 N_i(\xi, \eta) (\theta_x)_i \quad (16)$$

$$\theta_y = \sum_{i=1}^6 N_i(\xi, \eta) (\theta_y)_i \quad (17)$$

Similar to the membrane part, element strains for the bending part $\epsilon^k(\mathbf{u}^e)$ can be computed using Eqs. (16) and (17) in Eq. (4).

$$\epsilon^k(\mathbf{u}^e) = \mathbf{B}^b \mathbf{u}^e \quad (18)$$

where \mathbf{B}^b represents the element bending gradient matrix, and its nodal components \mathbf{B}_i^b for the i th node can be expressed as:

$$\mathbf{B}_i^b = \begin{bmatrix} 0 & 0 & 0 & -\frac{\partial N_i}{\partial x} & 0 \\ 0 & 0 & 0 & 0 & -\frac{\partial N_i}{\partial y} \\ 0 & 0 & 0 & -\frac{\partial N_i}{\partial y} & -\frac{\partial N_i}{\partial x} \end{bmatrix} \quad (i = 1, 2, \dots, 6) \quad (19)$$

Consequently, the element bending gradient matrix \mathbf{B}^b can be populated using \mathbf{B}_i^b for each node ($i = 1, 2, \dots, 6$) of the iTS6 inverse element.

$$\mathbf{B}^b = [\mathbf{B}_1^b \quad \mathbf{B}_2^b \quad \mathbf{B}_3^b \quad \mathbf{B}_4^b \quad \mathbf{B}_5^b \quad \mathbf{B}_6^b] \quad (20)$$

Finally, the element shear strain includes transverse deflection and bending rotations. Transverse deflection is interpolated using nodal deflections defined in terms of element basis functions.

$$w = \sum_{i=1}^6 N_i(\xi, \eta) (w_o)_i \quad (21)$$

Elemental shear strains $\gamma^o(\mathbf{u}^e)$ can now be computed using Eqs. (16), (17), and (21) in Eq. (5).

$$\gamma^o(\mathbf{u}^e) = \mathbf{B}^s \mathbf{u}^e \quad (22)$$

where \mathbf{B}^s represents the element shear gradient matrix and its component for the i th node can be written as:

$$\mathbf{B}_i^s = \begin{bmatrix} 0 & 0 & \frac{\partial N_i}{\partial x} & -N_i & 0 \\ 0 & 0 & \frac{\partial N_i}{\partial y} & 0 & -N_i \end{bmatrix} \quad (i = 1, 2, \dots, 6) \quad (23)$$

Finally, the complete element shear gradient matrix \mathbf{B}^s can be computed by concatenating \mathbf{B}_i^s for each node of the inverse element.

$$\mathbf{B}^s = [\mathbf{B}_1^s \quad \mathbf{B}_2^s \quad \mathbf{B}_3^s \quad \mathbf{B}_4^s \quad \mathbf{B}_5^s \quad \mathbf{B}_6^s] \quad (24)$$

An element based on FSDT assumptions, utilizing \mathbf{B}^s as the element shear strain gradient matrix, is susceptible to shear locking. Shear locking occurs when the element formulation assumes uniform shear strains through the thickness, which is an unrealistic assumption for thin plates. This phenomenon results in an artificially stiff response in bending, leading to inaccurate predictions of bending deformations.

2.5. Assumed shear strain field

Elements based on the FSDT often suffer from shear locking, and numerical results degrade significantly for thin plates. An easy workaround is to follow selective or reduced integration techniques; however, these techniques induce spurious mechanisms that can propagate themselves in the discretized domain. Therefore, the element can undergo deformations consistent with boundary

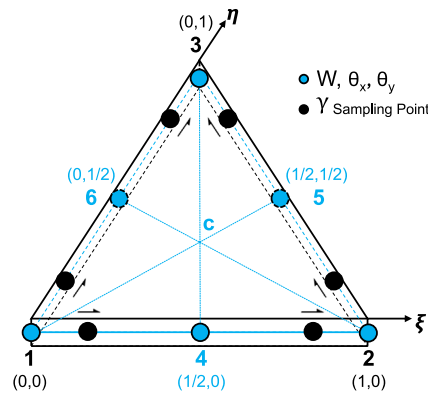


Fig. 2. Sampling points for assumed shear strain field.

conditions without consuming strain energy. Another tractable approach uses the assumed shear strain methodology [42–44] in formulating plate and shell elements. This approach has certain analogies with reduced integration techniques; however, full numerical integration, i.e., the Full Gauss Quadrature rules for triangles, helps overcome induced mechanisms and locking. The methodology involves sampling the original shear strain field at Gauss integration points and enforcing Kirchhoff’s assumptions.

Building upon Zienkiewicz’s formulation [42], transverse deflection and bending rotations are independently interpolated using standard quadratic basis functions. However, the transverse shear strain field is assumed to be linear and is interpolated using the following linear trial functions.

$$\gamma_\xi = \alpha_1 + \alpha_2 \xi + \alpha_3 \eta \tag{25}$$

$$\gamma_\eta = \alpha_4 + \alpha_5 \xi + \alpha_6 \eta \tag{26}$$

The coefficients α_i are evaluated by sampling the original shear strain field at the sampling points γ_s shown in Fig. 2. Following Zienkiewicz’s methodology [42], the substitutive transverse shear strain matrix can be expressed as follows:

$$\mathbf{B}_\gamma^s = \mathbf{N}_\gamma \mathbf{B}^s \tag{27}$$

Here, \mathbf{B}_γ^s is the substitutive matrix, and \mathbf{N}_γ represents the sampling-point basis function matrix which acts as an interpolation operator. It maps the values of the original element shear strain gradients \mathbf{B}^s , sampled at designated points within the element (as illustrated in Fig. 2), onto the linear variation defined by the trial functions γ_ξ and γ_η .

The substitutive matrix \mathbf{B}_γ^s now represents the modified element shear strain gradient matrix. The explicit form of the sampling-point basis functions \mathbf{N}_γ can be readily obtained from [42] or derived using the methodology outlined in Section 6.3.3 of [45].

2.6. Crack tip strain singularity

In computational fracture mechanics, specific element configurations can produce strain singularities and can be used to model crack tip behavior. Roshdy S. Barsoum [46] first presented this idea in quadratic isoparametric elements. Strain singularity refers to a situation where the strain field becomes infinite or undefined at a particular point within the finite element. While generally undesirable for most analyses, this behavior proves advantageous for problems involving elastic cracks.

An iTS6 inverse element can exhibit a $1/\sqrt{r}$ strain singularity by strategically repositioning mid-side nodes at the quarter points near the node 3 (as shown in Fig. 3). In an isoparametric element, the strain–displacement relation in terms of the element strain gradient matrix can be written as:

$$\{\epsilon^e\} = [\mathbf{J}]^{-1} \mathbf{B}^e \{\mathbf{u}^e\} \tag{28}$$

where ϵ^e and \mathbf{u}^e represent element strain and displacement fields, and \mathbf{B}^e shows the element general strain gradient matrix. In the above expression, the inverse of the Jacobian $[\mathbf{J}]^{-1}$ maps the generalized displacements defined in the natural coordinate system (ξ, η) to the global coordinate system (x, y) by the following mathematical expression.

$$\left\{ \begin{matrix} \frac{\partial N_i}{\partial x} \\ \frac{\partial N_i}{\partial y} \end{matrix} \right\} = [\mathbf{J}]^{-1} \left\{ \begin{matrix} \frac{\partial N_i}{\partial \xi} \\ \frac{\partial N_i}{\partial \eta} \end{matrix} \right\} \tag{29}$$

In Eq. (28), the displacements \mathbf{u}^e are bounded, and the general strain gradient matrix \mathbf{B}^e is defined using non-singular basis functions. Therefore, for strain singularity to exist, the singularity must arise from $[\mathbf{J}]^{-1}$. If the mid-side nodes are moved to the

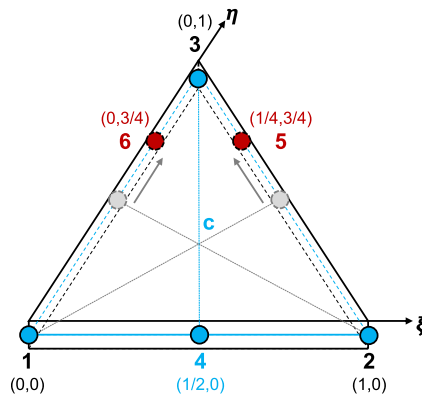


Fig. 3. Repositioning of mid-side nodes in the iTS6 master element.

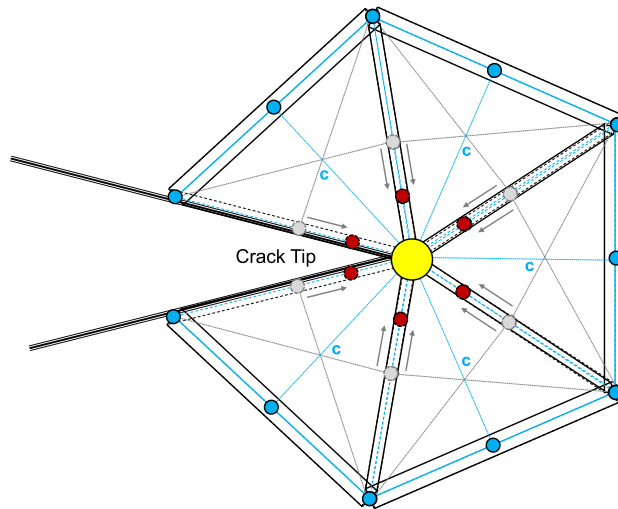


Fig. 4. Arrangement of quarter-point iTS6 inverse elements around the crack tip.

quarter point near node 3, located at the crack tip (as shown in Fig. 4), the Jacobian of the inverse element can be expressed as follows:

$$\mathbf{J} = \begin{bmatrix} \frac{\partial x}{\partial \xi} & \frac{\partial y}{\partial \xi} \\ \frac{\partial x}{\partial \eta} & \frac{\partial y}{\partial \eta} \end{bmatrix} = \begin{bmatrix} 1 - \eta_i & -\xi_i \\ 0 & 2(1 - \eta_i) \end{bmatrix} \tag{30}$$

In this equation, \mathbf{J} is Jacobian matrix, and (ξ_i, η_i) represents the nodal coordinates. The requirement of strain singularity can be achieved if the determinant of Jacobian is equal to zero for given nodal coordinates, which leads to $\mathbf{J}^{-1} = 0$.

$$|\mathbf{J}| = \frac{\partial(x, y)}{\partial(\xi, \eta)} = 0 \tag{31}$$

Evaluating the determinant of the Jacobian at all six nodal coordinates will result in singularity only at node-3 with nodal coordinates $(\xi_i = 0$ and $\eta_i = 1)$ as depicted in Fig. 3. This precisely controlled singularity significantly enhances accuracy in crack tip analysis, eliminating the need for excessively refined meshes near the crack tip. It is important to note that the singularity is strictly confined to the nodal point at the crack tip, and the strain variation within the inverse element is finite.

2.7. Strain sensor data

Strain sensor data is an integral part of any SHM methodology. The strain data obtained from onboard sensors represents the structural response to in-service operational and environmental loading conditions. This information is crucial in accessing structural integrity and implementing an effective SHM system. Since the iTS6 inverse shell element is developed for general loading conditions,

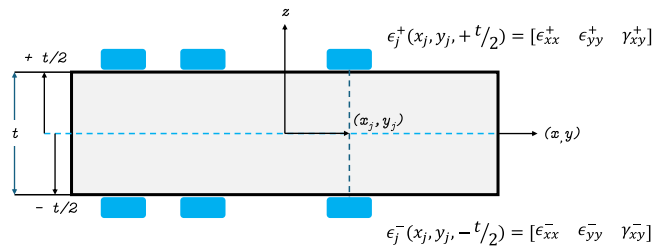


Fig. 5. Strain rosettes at discrete locations $(x_j, y_j, \pm \frac{t}{2})$.

the strain data from the top and bottom surface strain sensors are needed for general iFEM analysis. In contrast, strain sensors on either the top or bottom sides can suffice the requirements for pure in-plane and out-of-plane loading conditions.

In-situ strain data from onboard strain sensors (as shown in Fig. 5) can be represented in vector forms, constituting discrete strain measurements for membrane and bending strains.

$$e_j^* = \frac{1}{2} \begin{Bmatrix} \epsilon_{xx}^+ + \epsilon_{xx}^- \\ \epsilon_{yy}^+ + \epsilon_{yy}^- \\ \gamma_{xy}^+ + \gamma_{xy}^- \end{Bmatrix} \tag{32}$$

$$\kappa_j^* = \frac{1}{t} \begin{Bmatrix} \epsilon_{xx}^+ - \epsilon_{xx}^- \\ \epsilon_{yy}^+ - \epsilon_{yy}^- \\ \gamma_{xy}^+ - \gamma_{xy}^- \end{Bmatrix} \tag{33}$$

where e_j^* and κ_j^* represent discrete strain measures available via onboard strain sensors as compared to their numerically computed membrane and bending strain counterparts $\epsilon^o(\mathbf{u}^e)$ and $\epsilon^k(\mathbf{u}^e)$. The superscripts (+) and (-) associate the strain measures with the strain rosettes located on the top and bottom surfaces of the plate, respectively.

In-situ strain measurements obtained from onboard strain sensors are pivotal in iFEM formulation. Experimental section strains can be computed using these measurements at discrete locations within the elemental geometric domain (x_j, y_j) at the mid-plane. Due to their negligible effect, experimental transverse shear strains Γ_j^* are typically neglected for thin plate and shell structures. However, when transverse deformation effects are considered, transverse shear strains can be readily calculated using in-situ strain measurements (e_j^*, κ_j^*) in conjunction with the equilibrium equations provided by First-order Shear Deformation Theory (FSDT).

2.8. Weighted least squares functional

The iFEM framework is built on the principle of the variational method which reconstructs the displacement field by minimizing the weighted least squares error functional. The error functional is formulated using discrete strain measures and their corresponding numerical counterparts in a discretized geometric domain. A significant benefit of the iFEM scheme is its independence from elastic or inertial material properties and loading conditions for full-field shape reconstruction.

The weighted least squares functional for the proposed ITS6 inverse element is defined as the sum of the error terms between the numerically computed strains and the discretely measured strain values over the discretized element domain.

$$\phi(\mathbf{u}^e) = \phi_m(\mathbf{u}^e) + \phi_b(\mathbf{u}^e) + \phi_s(\mathbf{u}^e) \tag{34}$$

where

$$\phi_m(\mathbf{u}^e) = w_e \|\epsilon^o(\mathbf{u}^e) - e^*\|^2$$

$$\phi_b(\mathbf{u}^e) = w_\kappa \|\epsilon^k(\mathbf{u}^e) - \kappa^*\|^2$$

$$\phi_s(\mathbf{u}^e) = w_\Gamma \|\gamma^o(\mathbf{u}^e) - \Gamma^*\|^2$$

Here w_e , w_κ , and w_Γ are the weighting coefficients associated with the functional error corresponding to the membrane, bending, and shear errors, respectively. Each of the squared norms defined in Eq. (34) can be further expressed over the inverse element domain Ω^{iel} as:

$$\|\epsilon^o(\mathbf{u}^e) - e^*\|^2 = \iint_{A_e} \left(\epsilon^o(\mathbf{u}^e) - e^* \right)^2 dx dy$$

$$\|\epsilon^k(\mathbf{u}^e) - \kappa^*\|^2 = \iint_{A_e} \left(\epsilon^k(\mathbf{u}^e) - t^2 \kappa^* \right)^2 dx dy$$

$$\|\gamma^o(\mathbf{u}^e) - \Gamma^*\|^2 = \iint_{A_e} \left(\gamma^o(\mathbf{u}^e) - \Gamma^* \right)^2 dx dy$$

where A_e is the area of the inverse element.

The weighting coefficients w_e , w_κ , and w_Γ defined in error functional balance the influence of available discrete strain measures in the closed-form solution. Setting the coefficients to unity gives equal importance to all data points, known with certainty when the strain measures are available. In contrast, setting the coefficients to a minimal value ($10^{-3} - 10^{-6}$) when the strain data is missing reduces the impact of these missing data points during the error minimization process, preventing them from unduly affecting the overall result. This approach helps to ensure that the iFEM algorithm exhibits robustness and reliability in computing displacement profiles even with sparse arrangements of strain sensors, making them valuable for real-world shape sensing and SHM applications.

Minimizing the weighted least squares error functional in Eq. (34) with respect to the unknown nodal displacements \mathbf{u}^e of an inverse element reduces to the normal equation of the form:

$$\frac{\partial \phi(\mathbf{u}^e)}{\partial \mathbf{u}^e} = \mathbf{m}^e \mathbf{u}^e - \mathbf{s}^e = 0 \quad (35)$$

and the equilibrium equation can now be written as:

$$\mathbf{m}^e \mathbf{u}^e = \mathbf{s}^e \quad (36)$$

where \mathbf{m}^e represents the error minimization matrix, \mathbf{s}^e is the measured strain vector comprising discrete strain measures obtained from the onboard strain sensors, and \mathbf{u}^e is the unknown nodal displacements to be determined after prescribing necessary displacement boundary conditions.

The mathematical expression for \mathbf{m}^e and \mathbf{s}^e can be further derived by substituting Eqs. (13), (18) and (22) in Eq. (35).

$$\mathbf{m}^e = \mathbf{m}_m^e + \mathbf{m}_b^e + \mathbf{m}_s^e \quad (37)$$

where

$$\begin{aligned} \mathbf{m}_m^e &= \iint_{A_e} \left(w_e (\mathbf{B}^m)^T \mathbf{B}^m \right) dx dy \\ \mathbf{m}_b^e &= \iint_{A_e} \left((t^2) w_\kappa (\mathbf{B}^b)^T \mathbf{B}^b \right) dx dy \\ \mathbf{m}_s^e &= \iint_{A_e} \left(w_\Gamma (\mathbf{B}_\gamma^s)^T \mathbf{B}_\gamma^s \right) dx dy \end{aligned}$$

Notably, error minimization matrices (\mathbf{m}_m^e , \mathbf{m}_b^e , \mathbf{m}_s^e) are independent of material properties. The measured strain vector \mathbf{s}^e is written as:

$$\mathbf{s}^e = \mathbf{s}_m^e + \mathbf{s}_b^e + \mathbf{s}_s^e \quad (38)$$

where

$$\begin{aligned} \mathbf{s}_m^e &= \iint_{A_e} \left(w_e (\mathbf{B}^m)^T \mathbf{e}^* \right) dx dy \\ \mathbf{s}_b^e &= \iint_{A_e} \left((t^2) w_\kappa (\mathbf{B}^b)^T \boldsymbol{\kappa}^* \right) dx dy \\ \mathbf{s}_s^e &= \iint_{A_e} \left(w_\Gamma (\mathbf{B}_\gamma^s)^T \boldsymbol{\Gamma}^* \right) dx dy \end{aligned}$$

Eq. (37) computes the elemental equations for the iTS6 inverse element. For global analysis, these equations are compiled into a global system of equations after necessary transformations from local to global coordinate system.

2.9. Coordinate transformation system

Shell elements help model curved surfaces by combining flexural and in-plane behavior. If the shell elements are two-dimensional, the flexural and in-plane states are naturally decoupled at the element level for homogeneous materials. However, flexural-membrane coupling emerges when the global coordinate system assembles flat elements meeting at different angles, as shown in Fig. 6. Despite being inherently two-dimensional, these elements can effectively approximate curved surfaces in a discretized space. Typically, two-dimensional shell elements, formulated by superpositioning membrane and bending elements, are computationally efficient and have reduced complexity. Therefore, the transformation between the element local and global coordinate system is crucial to two-dimensional shell formulations, i.e., the proposed inverse shell element.

Consider the iTS6 element defined in a local coordinate system, as illustrated in Fig. 1. Knowing the position vectors defined by any two nodes within the element, the unit vectors representing the local coordinate system (x', y', z') can be readily determined using vector calculus.

$$\mathbf{V}_{ij}^e = \begin{Bmatrix} x_j - x_i \\ y_j - y_i \\ z_j - z_i \end{Bmatrix}^e = \begin{Bmatrix} x_{ij} \\ y_{ij} \\ z_{ij} \end{Bmatrix}^e \quad (39)$$

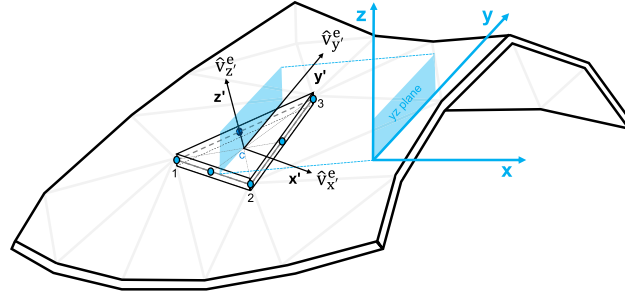


Fig. 6. Shell element defined in local coordinate system.

The unit vector is

$$\hat{\mathbf{v}}_{ij}^e = \frac{1}{l_{ij}^e} \begin{Bmatrix} x_{ij} \\ y_{ij} \\ z_{ij} \end{Bmatrix}^e = \frac{\mathbf{V}_{ij}^e}{\|\mathbf{V}_{ij}^e\|} \quad (40)$$

where the length of side ij .

$$l_{ij}^e = \sqrt{(x_{ij}^2 + y_{ij}^2 + z_{ij}^2)}^e$$

Let us start from the unit normal along the local z' axis. For the iTS6 inverse element, the transverse local unit vector is determined using Eqs. (39) and (40).

$$\hat{\mathbf{v}}_{z'}^e = \frac{\mathbf{V}_{12}^e \times \mathbf{V}_{13}^e}{\|\mathbf{V}_{12}^e \times \mathbf{V}_{13}^e\|} = \begin{Bmatrix} \lambda_{z'x} \\ \lambda_{z'y} \\ \lambda_{z'z} \end{Bmatrix}^e \quad (41)$$

where \mathbf{V}_{12} and \mathbf{V}_{13} represent in-plane position vectors along nodes 1–2 and 1–3, respectively. The local y' axis is now defined by intersecting the element with a plane parallel to the global yz plane, as shown in Fig. 6.

$$\hat{\mathbf{v}}_{y'}^e = \begin{Bmatrix} 0 \\ \lambda_{y'y} \\ \lambda_{y'z} \end{Bmatrix}^e \quad (42)$$

where the projection of x' along the global y axis is zero. The unknown components $(\lambda_{y'y}, \lambda_{y'z})$ of the unit vector $\hat{\mathbf{v}}_{y'}^e$, along y' and z' axis can now be determined from the facts that the length of this vector is unity.

$$\left(\lambda_{y'y}^e\right)^2 + \left(\lambda_{y'z}^e\right)^2 = 1 \quad (43)$$

and the second necessary equation comes from the condition that the scalar product of the unit vectors $\hat{\mathbf{v}}_{y'}^e$ and $\hat{\mathbf{v}}_{z'}^e$ is zero.

$$\lambda_{y'y}^e \lambda_{z'y}^e + \lambda_{y'z}^e \lambda_{z'z}^e = 0 \quad (44)$$

From Eqs. (43) and (44), the unknown components $(\lambda_{y'y}, \lambda_{y'z})$ of the unit vector $\hat{\mathbf{v}}_{y'}^e$ can be obtained easily.

$$\lambda_{y'y}^e = \frac{1}{\sqrt{1 + \left(\frac{\lambda_{z'z}^e}{\lambda_{z'y}^e}\right)^2}}$$

$$\lambda_{y'z}^e = \frac{1}{\sqrt{1 + \left(\frac{\lambda_{z'y}^e}{\lambda_{z'z}^e}\right)^2}}$$

Consequently, the unit vector in the direction of local x' axis is obtained by the cross product of $\hat{\mathbf{v}}_{y'}^e$ and $\hat{\mathbf{v}}_{z'}^e$.

$$\hat{\mathbf{v}}_{x'}^e = \hat{\mathbf{v}}_{y'}^e \times \hat{\mathbf{v}}_{z'}^e = \begin{Bmatrix} \lambda_{x'x} \\ \lambda_{x'y} \\ \lambda_{x'z} \end{Bmatrix}^e \quad (45)$$

The local unit vectors $(\hat{\mathbf{v}}_{x'}^e, \hat{\mathbf{v}}_{y'}^e, \hat{\mathbf{v}}_{z'}^e)$ are essentially the direction cosines that describe the orientation of the local coordinate system $[x', y', z']$ relative to the global coordinate system $[x, y, z]$. Finally, the transformation matrix can be populated using the direction

cosines presented in Eqs. (41), (42), and (45) as:

$$T = \begin{pmatrix} \lambda_{x'x}^e & \lambda_{x'y}^e & \lambda_{x'z}^e \\ \lambda_{y'x}^e & \lambda_{y'y}^e & \lambda_{y'z}^e \\ \lambda_{z'x}^e & \lambda_{z'y}^e & \lambda_{z'z}^e \end{pmatrix} \quad (46)$$

Here, T is a 3×3 transformation matrix for the transformation of global coordinates $[x, y, z]$ to the local coordinates, i.e., $[x', y', z'] = T[x, y, z]$. This transformation is pivotal to two-dimensional shell formulations to ensure accurate alignment of the local and global coordinate systems.

In the iTS6 inverse element, the presence of mid-side nodes enhances interpolation capabilities and implicitly provides additional degrees of freedom to improve interelement continuity and compatibility. To undertake the iFEM analysis of buildup structures, introducing artificial inplane rotation DOF effectively addresses the challenges associated with quasi-coplanar nodes in mapping buildup structures with two-dimensional shell elements. This approach ensures computational efficiency while maintaining the accuracy and stability of the iTS6 inverse element in capturing the complex behavior of curved shell structures. Following this technique, the local displacement field for the proposed inverse element can be rewritten in the local coordinate system by including additional artificial rotation θ'_z as:

$$\bar{\mathbf{u}}_i^e = \begin{Bmatrix} (u'_o)_i \\ (v'_o)_i \\ (w'_o)_i \\ (\theta'_x)_i \\ (\theta'_y)_i \\ (\theta'_z)_i \end{Bmatrix} \quad (i = 1, 2, \dots, 6) \quad (47)$$

In order to maintain 6-DOFs at all nodes, an arbitrary coefficient m'_{θ_z} is added to the diagonal term of the local numerical shape matrix already defined in Eq. (37).

$$\bar{\mathbf{m}}_{ij6 \times 6}^e = \begin{bmatrix} \mathbf{m}_{ij5 \times 5}^e & \vdots & 0 \\ \dots & \vdots & \dots \\ 0 & \vdots & m'_{\theta_z} \end{bmatrix} \quad (48)$$

The value of the artificial stiffness matrix m'_{θ_z} is typically chosen in the order of EtA^e [47]. The numerical results have consistently established minimal sensitivity to the artificial rotation stiffness due to its uncoupled contribution in the shape matrix presented in Eq. (48). The modified local numerical shape matrix $\bar{\mathbf{m}}_{ij}^e$ is then transformed into global axes using the standard method, resulting in non-singular global equations.

$$\mathbf{m}_{ij}^e = [T^e]^T \bar{\mathbf{m}}_{ij6 \times 6}^e [T^e] \quad (49)$$

where T^e represents an element transformation matrix. For the entire iTS6 inverse shell element, which now has six DOFs per node, the complete element transformation matrix can be formulated as:

$$T^e = \begin{bmatrix} T & & & & & \\ & T & & & & 0 \\ & & T & & & \\ & & & T & & \\ sym & & & & T & \\ & & & & & T \end{bmatrix} \quad (50)$$

The element transformation matrix T^e is a block-diagonal matrix used to transform local element stiffness matrices to the global coordinate system, and the transformation matrix T is already defined in Eq. (46). The element transformation matrix's 36×36 structure is essential for accurately mapping the local stiffness contributions to the global system, especially in three-dimensional problems where each node has six DOFs (three translations and three rotations).

2.10. Global assembly and solution

The element contributions defined in Eqs. (37) and (38) can be assembled in the global system after appropriate coordinate transformations as:

$$\mathbf{M}\mathbf{U} = \mathbf{S} \quad (51)$$

$$\text{and } \mathbf{M} = \sum_{e=1}^{N_{iel}} \mathbf{m}^e, \quad \mathbf{U} = \sum_{e=1}^{N_{iel}} \mathbf{u}^e, \quad \mathbf{S} = \sum_{e=1}^{N_{iel}} \mathbf{s}^e$$

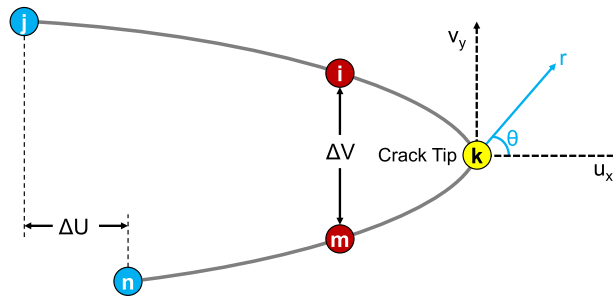


Fig. 7. Crack tip displacement path for a full-model crack.

Consequently, \mathbf{M} , \mathbf{U} , and \mathbf{S} imply the global error minimization matrix, unknown displacement vector, and measured strain vector in iFEM formulation. N_{iel} represents the total number of inverse elements in the discretized structural domain. After prescribing the essential boundary conditions, the partitioned global system of equations can be written as:

$$\mathbf{M}_p \mathbf{U}_p = \mathbf{S}_p \tag{52}$$

In the end, unknown nodal displacements \mathbf{U}_p can be computed by solving a pertained system of equations via conventional FEM solution techniques to realize full-field reconstruction displacement profiles.

After obtaining the displacement field, we can use the nodal displacements to calculate the stress intensity factors (SIFs). For the proposed iTS6 inverse shell element, three types of Stress Intensity Factors (SIFs) can be calculated at a crack tip: the opening SIF K_I , which results from normal stress causing the crack faces to separate perpendicularly (Mode I); the in-plane shear SIF K_{II} , which arises from shear stress causing the crack faces to slide over each other within the plane of the crack (Mode II); and the tearing SIF K_{III} , which is due to out-of-plane shear stress causing the crack faces to slide relative to each other in a direction perpendicular to the crack plane (Mode III). These SIFs are crucial for quantifying the stress state near the crack tip, enabling accurate predictions of crack growth and potential failure.

Fig. 7 shows the crack tip displacement path for a full crack model, illustrating the nodes around the crack tip in a planar element. The diagram shows several key nodes labeled i , j , k , m , and n , with the crack tip located at node k . The crack tip is situated at the origin of the local cylindrical coordinate system, where the radial distance $r = 0$ and the angle θ are measured from the positive x -axis. Now, for the nodes positioned on the crack surface, specifically at $\theta = 180^\circ$ (directly on the opposite side of the crack plane), the SIFs can be calculated using displacement extrapolation method [48].

$$K_I = \sqrt{2\pi} \frac{G}{1 + E_b} \frac{|\Delta V|}{\sqrt{r}} \tag{53}$$

$$K_{II} = \sqrt{2\pi} \frac{G}{1 + E_b} \frac{|\Delta U|}{\sqrt{r}} \tag{54}$$

$$K_{III} = \sqrt{2\pi} \frac{G}{1 + E_b} \frac{|\Delta W|}{\sqrt{r}} \tag{55}$$

where K_I , K_{II} , and K_{III} represent the stress intensity factors for Modes I, II, and III, respectively. The terms ΔU , ΔV , and ΔW represent the relative displacements along the horizontal, lateral, and transverse directions for the nodes adjacent to the crack tip. The shear modulus G can be calculated using the elastic modulus E and Poisson's ratio ν . The bulk modulus E_b differs depending on the in-plane loading conditions: for plane stress $E_b = (3 - \nu)/(1 + \nu)$ and plane strain, $E_b = 3 - 4\nu$. The crack propagation angle in terms of SIFs can be expressed as:

$$\theta = \cos^{-1} \left(\frac{3K_{II}^2 + K_I \sqrt{K_I^2 + 8K_{II}^2}}{K_I^2 + 9K_{II}^2} \right) \tag{56}$$

The G-criterion is used to predict material failure by relating the critical stress intensity factor (K_c) to the stress intensity factors for different crack loading modes. The criterion is expressed by the following equation:

$$K_c^2 = K_I^2 + K_{II}^2 + \frac{E'}{2G} K_{III}^2 \tag{57}$$

where the effective modulus E' is given by $E' = E/(1 - \nu^2)$ for plane strain conditions and $E' = E$ for plane stress conditions. This criterion enables accurate failure prediction by integrating the effects of different loading modes, considering the material's response under varying stress conditions.

The terms $|\Delta V|/\sqrt{r}$, $|\Delta U|/\sqrt{r}$ and $|\Delta W|/\sqrt{r}$ defined in Eqs. (53), (54), and (55) are assumed to be linear at the crack surface and can be obtained at $r \rightarrow 0$ for the crack tip as:

$$\frac{|\Delta V|}{\sqrt{r}} = \frac{|\Delta V_{im}|(d_2)^{\frac{3}{2}} - |\Delta V_{jn}|(d_1)^{\frac{3}{2}}}{\sqrt{d_1 d_2} (d_2 - d_1)}$$

$$\frac{|\Delta U|}{\sqrt{r}} = \frac{|\Delta U_{im}|(d_2)^{\frac{3}{2}} - |\Delta U_{jn}|(d_1)^{\frac{3}{2}}}{\sqrt{d_1 d_2}(d_2 - d_1)}$$

$$\frac{|\Delta W|}{\sqrt{r}} = \frac{|\Delta W_{im}|(d_2)^{\frac{3}{2}} - |\Delta W_{jn}|(d_1)^{\frac{3}{2}}}{\sqrt{d_1 d_2}(d_2 - d_1)}$$

For a full crack model (as shown in Fig. 7), the relative displacements are calculated as $\Delta V_{im} = v_i - v_m$, $\Delta U_{im} = u_i - u_m$ and $\Delta W_{im} = w_i - w_m$, where (u_i, v_i) , (u_m, v_m) and (w_m, w_m) are the horizontal, lateral, and transverse displacements computed at nodes i and m via iFEM analysis. Similarly, the relative displacements ΔU_{jn} , ΔV_{jn} , and ΔW_{jn} can be calculated. Here, d_1 is the distance between nodes k and i (or k and m), and d_2 is the distance between nodes k and j (or k and n).

Displacement-based SIF calculation is particularly suited for shape sensing analysis because it directly uses measurements obtained from reconstructed displacement fields. This approach integrates seamlessly within the framework of iFEM, eliminating the need for additional transformations and enabling immediate interpretation of sensor data in real-time SHM applications, providing timely insights about structural health.

3. Numerical validation and analysis

The iFEM formulation of the proposed inverse element is numerically validated by considering various cases in the following section. Since all numerical models are based on certain assumptions or simplifications, their validation against analytical solutions helps to verify the validity of these assumptions and ensures that they do not introduce significant errors. On the contrary, if analytical solutions are not readily available, establishing an equivalent structural state is mandatory for numerical validation. As a consequence, the computation of equivalent displacements can help to validate iFEM results against FEM reference solutions to ensure that the numerical results are reliable and can be used confidently for real-world applications. The total equivalent displacement can be computed as:

$$U_{eq} = \sqrt{u^2 + v^2 + w^2} \quad (58)$$

where u , v , and w are the longitudinal, lateral, and transverse displacements along x , y , and z axis, respectively. Furthermore, to investigate the accuracy of iFEM results, the percent-difference between the reconstructed displacements (i.e., equivalent displacements) and FEM reference solution can be calculated as:

$$Percent\ Difference\ (\%) = \left| \frac{U_{eq}^{iFEM} - U_{eq}^{Ref}}{U_{eq}^{Ref}} \right| \times 100 \quad (59)$$

and variables U_{eq}^{iFEM} and U_{eq}^{Ref} imply equivalent displacements computed via iFEM analysis and its reference solution computed through high-fidelity FEM analysis.

The availability of discrete surface strain measures is an integral part of the iFEM analysis, and the kind of data is obtained from the onboard strain sensors installed on the engineering structures. In contrast, synthetic strain data can be obtained through high-fidelity forward FEM analysis. Under similar loading and boundary conditions, the strain data acquired through FEM analysis can reliably duplicate the experimental strain data obtained from the experimental setup. Since FEM is a well-established analysis technique, the numerical validation of inverse formulations via synthetic strain data is widely accepted in the literature. In the current study, discrete strain measures are obtained via high-fidelity FEM simulations, which is equivalent to the placement of the strain rosette at an appropriate location in the iFEM discretized element.

In industrial applications, the decision on the number of sensors needed for shape sensing is governed by several factors. These include space availability for sensor installation, financial constraints, existing health of the structural systems, computational accuracy, and efficiency requirements. Optimal sensor arrangement can be achieved by optimizing the iFEM scheme for inverse element discretization, sensor locations within the inverse element spatial domain, and weighting functions associated with the weighted least squares error functional. Additionally, techniques such as sensor fusion and advanced signal processing can further enhance the robustness of iFEM analysis with fewer sensors. It is important to note that these optimizations are specific to each structural system, and therefore, a unique closed-form solution does not exist to obtain an optimal sensor arrangement.

In this study, the numerical validation considered two sensor arrangements, which are identified as dense and sparse sensor arrangements. These sensor arrangements are utilized to validate the proposed inverse formulation through iFEM analysis. In dense sensor arrangements, strain rosettes are assumed to be present in the elemental domain of each inverse element within the discretized space. In this case, the iFEM setup represents a typical inverse problem, and the variational principle does not govern the analysis because none of the sensors is missing in any elemental domain. Therefore, the iFEM results obtained with dense sensor arrangement are used to validate the accuracy of the inverse formulation against reference solutions. Meanwhile, sparse sensor arrangements arbitrarily represent a real-world scenario where few sensors cover the entire discretized space, and most inverse elemental domains are empty. The iFEM analysis for sparse arrangement is dominated by variational weighted least squares functional, and the iFEM results obtained via this arrangement are used to validate the robustness of the iFEM formulation by arbitrarily employing fewer sensors.

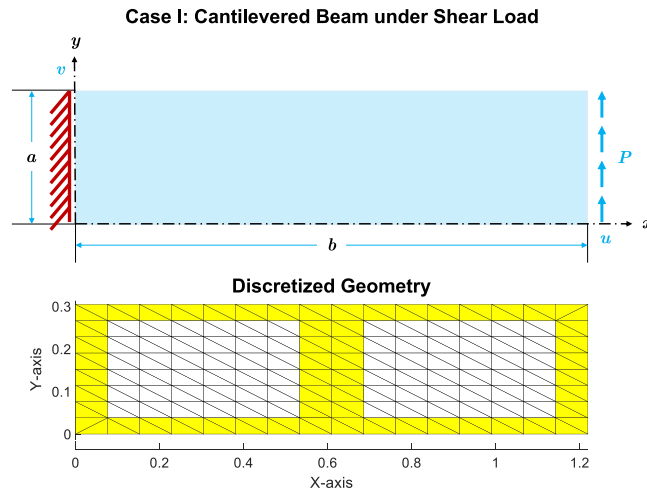


Fig. 8. Case I: Cantilevered beam with free edge under shear load and discretized geometric domain.

A detailed numerical validation plan includes iFEM analysis of structures with and without preexisting cracks. First, benchmark cases without cracks will be evaluated to assess the accuracy of the proposed inverse formulation for reconstructing longitudinal, lateral, and transverse deformation profiles. Next, two cases with preexisting cracks will be assessed to extend the application of iFEM analysis in fracture mechanics. This comprehensive approach will verify the shape sensing capability of the iTS6 inverse element for real-time SHM applications in shell structures, both with and without existing cracks.

3.1. Structures without crack

It is essential to emphasize that the location of strain sensors within the inverse element domain and the values of weighting coefficients w_e , w_k , and w_Γ are critical to the variational formulation of iFEM. In subsequent numerical validation cases, the location of the strain sensors is fixed at the centroid of each inverse element. Also, for missing in-situ discrete strain measures, the values for weighting coefficients are set to $w_e = w_k = w_\Gamma = 10^{-4}$ to ensure standardization in the analysis setup. Sparse sensor arrangements are assumed to have significantly fewer sensors than dense arrangements. The aim, however, remains to analyze the accuracy and robustness of the proposed inverse formulation using fewer sensors while keeping all other variable factors constant, i.e., discretization, sensor locations, and weighting functions. This approach minimizes variations and simplifies comparative analysis of iFEM results across different numerical validation cases.

3.1.1. Beam under inplane loading (Case I)

In the literature, the shear-loaded cantilever beam presented by Timoshenko [49] is commonly used as a benchmark problem to validate the in-plane response of new elements. In this context, we are revisiting this problem to assess the inplane response capability of the newly developed inverse element.

Consider a rectangular beam with length $a = 1.2192$ m and width $b = 0.3048$ m, as illustrated in Fig. 8. The beam has a constant cross-sectional area with a thickness of $t = 25.4$ mm. The left edge of the beam is fixed, and the right edge is subjected to a resultant shear loading of $P = 177.929$ kN. The beam is made of a uniform and isotropic material with the elastic modulus $E = 206.84$ GPa and Poisson's ratio $\nu = 0.25$. According to the elasticity solution, the maximum lateral displacement at the upper corner of the free edge beam is given as:

$$v_y = \frac{4Pb^3}{Eta^3} + \frac{2(4+5\nu)Pb}{4Eta} = 9.025 \text{ mm} \quad (60)$$

First, a high-fidelity FEM analysis is performed using an in-house solver with a structured mesh of 256 uniformly distributed triangular elements. The maximum lateral displacement of $v_y = 9.053$ mm is observed at the right top corner of the beam (as shown in Fig. 9a), which is in close agreement with the elasticity solution mentioned in Eq. (60). Also, the maximum longitudinal displacement of $v_x = 1.632$ mm is observed at the free end of the beam (as shown in Fig. 10a). The displacement profiles from the FEM solution are then used to synthesize the strain data measures for subsequent shape sensing analysis within the framework of iFEM.

In dense sensor arrangement, strain rosettes are placed in all inverse elements in the entire geometric domain, as shown in Fig. 8. Whereas, in a sparse sensor arrangement, strain sensors are placed at specific inverse elements along the highlighted yellow path. The results from both iFEM scenarios accurately reconstruct deformation profiles, and the maximum lateral displacements closely match the reference solution. The errors are 0.93% and 2.32% for dense and sparse iFEM analyses (as shown in Fig. 9b and c),

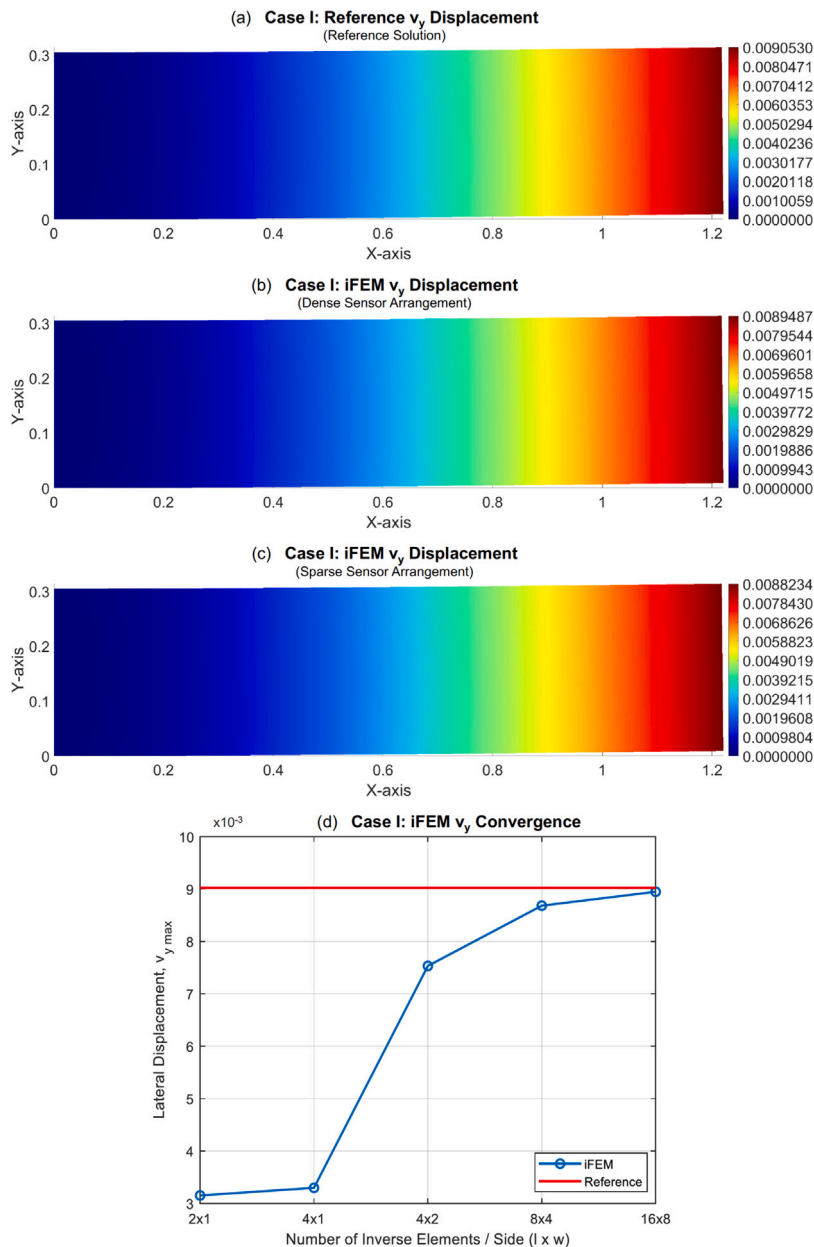


Fig. 9. Case I: Lateral displacement profiles for FEM reference solution, iFEM solution (dense-sensor), iFEM solution (sparse-sensor), and iFEM convergence chart for the lateral reconstructed displacement profile.

respectively, when compared to the analytical results. Additionally, the lateral displacement contours from both FEM and iFEM analyses are indistinguishable, showing maximum deflection at the right edge of the cantilever beam.

The longitudinal displacement profiles for dense and sparse sensor arrangements are similar to the reference solution (as shown in Fig. 10). The reconstructed displacement contours of u_x accurately predict symmetric squeezing and stretching along the upper and lower edges of the cantilever beam under an upward shear load at the free edge. Maximum longitudinal displacements for the dense and sparse iFEM analyses are 1.623 mm and 1.616 mm (as shown in Fig. 10b and c), respectively, compared to the maximum longitudinal displacement of 1.632 mm obtained in the reference solution.

The influence of discretization on iFEM analysis is studied (as shown in Figs. 9d and 10d) to evaluate how different mesh densities effect the displacement reconstruction accuracy. The convergence charts for longitudinal and lateral displacements indicate that the iFEM solutions consistently approach the reference solutions as the number of inverse elements increases. The iFEM mesh with 16×8 inverse elements per side (with 256 inverse elements) converges monotonically to the reference solution.

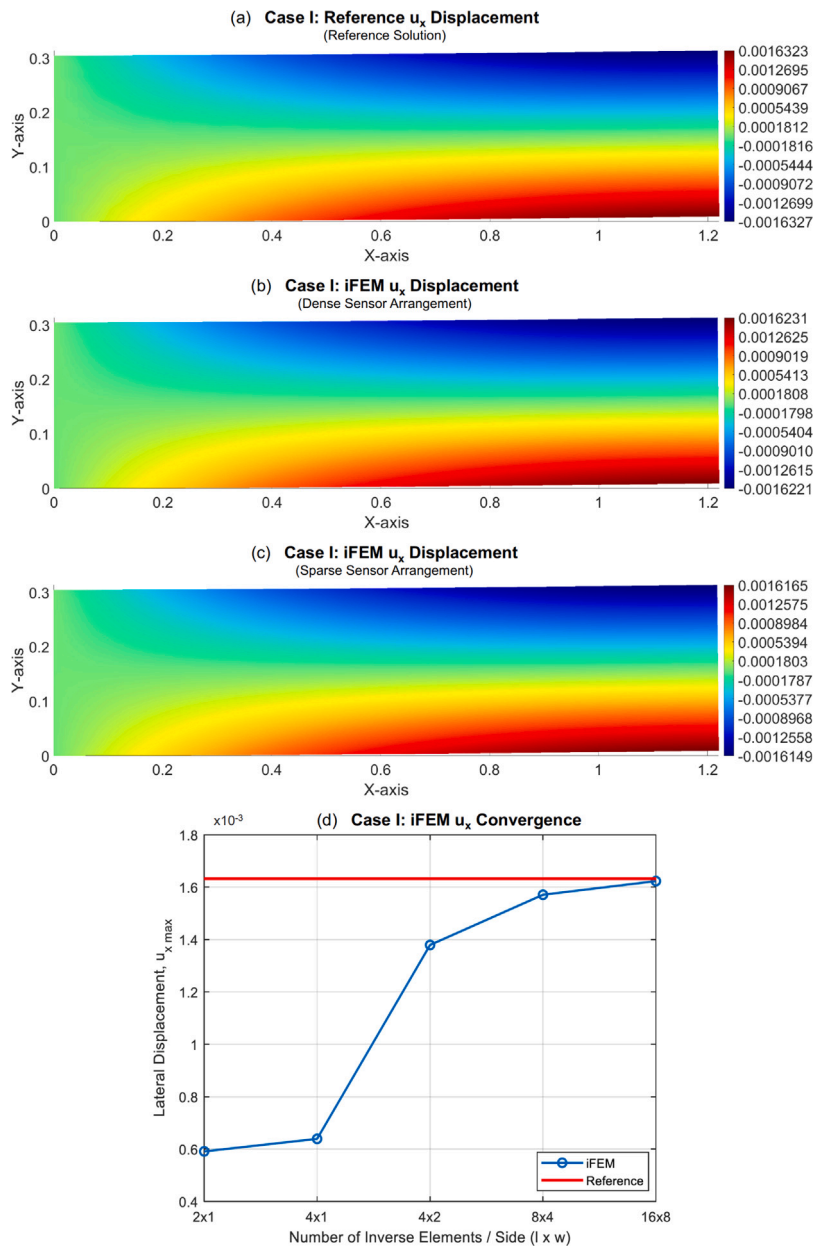


Fig. 10. Case I: Longitudinal displacement profiles for FEM reference solution, iFEM solution (dense-sensor), iFEM solution (sparse-sensor), and iFEM convergence chart for the longitudinal reconstructed displacement profile.

Furthermore, the iFEM convergence graph demonstrates that an 8×4 discretization arrangement with 64 inverse elements can reconstruct displacement profiles with over 95% accuracy. This configuration reduces the sensor count by approximately 75%, significantly decreasing computational effort while maintaining acceptable accuracy. Optimized discretization is essential for the practical applicability and computational feasibility of iFEM analysis in real-time shape sensing and SHM applications. The in-plane response of the iTS6 inverse element is successfully validated in the current case, and details for the given case are summarized in Table 1.

3.1.2. Radial loading on cylindrical shell (Case II)

The pinched cylinder with a diaphragm is a well-known benchmark and is considered one of the most severe tests for both inextensional bending modes and complex membrane states. It is also part of the “obstacle course for shell elements” [50]. The cylinder, with a length $l = 600$, radius $r = 300$, and thickness $t = 3$, is subjected to a unit point load $P = 1$ at the center on opposite sides, as illustrated in Fig. 11. The cylinder has rigid end diaphragms; its material properties are $E = 3.0 \times 10^6$ and $\nu = 0.3$.

Table 1
Analysis details of Case - I.

Analysis (Type)	Sensor (Arrangement)	max u_x (mm)	max v_y (mm)	Err u_x (Abs%)	Err v_y (Abs%)
iFEM	Dense	1.623	8.948	0.56	0.93
iFEM	Sparse	1.616	8.823	0.97	2.32
Reference Solution					
Analysis	Elements	u max	v max		
FEM	224	1.632 mm	9.053 mm		
Analytical	-	-	9.025 mm [49]		

Case II: Pinched Cylinder with Diaphragm

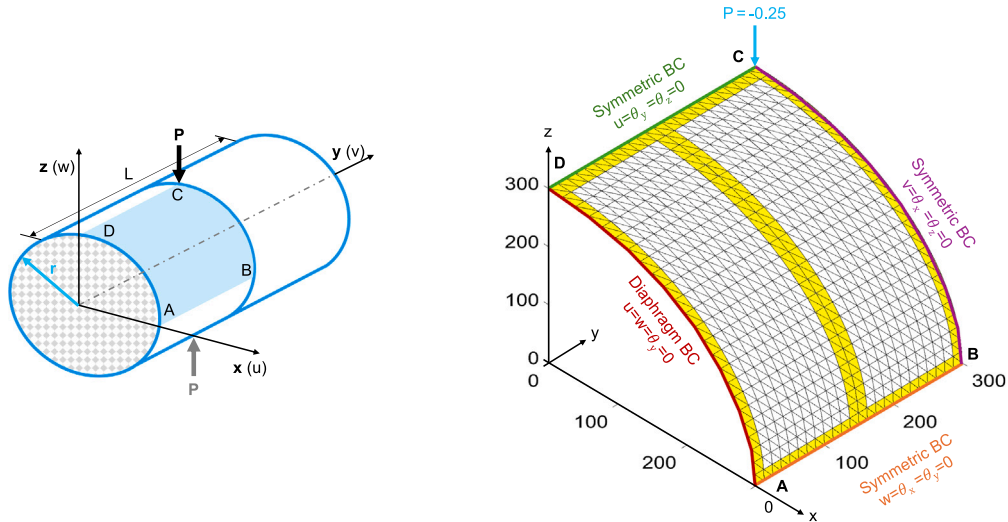


Fig. 11. Case II: Pinched cylinder benchmark test and discretized geometry depicted with loading and boundary conditions.

Due to the problem's symmetry, only one octant of the cylinder is analyzed using FEM and iFEM analysis (as shown in Fig. 11). The discretized geometry is subjected to symmetric boundary conditions along the sides AB, BC, and CD, whereas it is subjected to rigid diaphragm boundary conditions along the AB end. A radial point load of -0.25 is applied on the corner at point C. The analytical solution for this case results in a maximum transverse displacement of $w_z = -1.8248 \times 10^{-5}$ at the point of load application.

High-fidelity FEM analysis is conducted using a structured discretization of 1152 uniformly distributed triangular elements to replicate the analytical result. The numerical solution successfully converges to the analytical solution and shows the maximum transverse displacement of -1.821×10^{-5} . The maximum displacement appears at a highly localized place (as depicted in Fig. 12a), precisely at the node where the radial point load is applied. This localized displacement is due to the concentrated nature of the load, which causes a significant deformation at the point of application. Synthetic strain data is generated based on the displacement profile obtained from the high-fidelity model for subsequent shape sensing analysis. Two iFEM scenarios, using dense and sparse sensor arrangements, are considered to evaluate the accuracy and robustness of the proposed inverse formulation, respectively. The dense arrangement assumes that synthetic strain measures are available to all inverse elements in the discretized geometry (as shown in Fig. 11), and for sparse arrangement, the synthetic strain sensors are assumed to be placed only in the inverse elements highlighted in yellow.

The shape sensing displacement profile reconstructed during the iFEM analysis for both dense and sparse sensor arrangements closely matches the reference displacement profile obtained from the high-fidelity model. The maximum transverse deflection observed for the dense sensor arrangement is 1.754×10^{-5} , (as shown in Fig. 12b). Given the complexity and nature of the problem, the iFEM result correlates well with the analytical solution, with an observed absolute error of 3.88%. In the sparse sensor arrangement, less than 25% of strain sensors are used to reconstruct the full-field displacement profile. The transverse displacement obtained from the sparse sensor arrangement is 1.724×10^{-5} , with an observed absolute error of 5.523%, (as shown in Fig. 12c). The iFEM displacement contours from dense and sparse sensor arrangements are indistinguishable from the reference solution.

The effect of inverse discretization on the reconstruction of displacement profiles is also studied, and the iFEM convergence chart is presented in Fig. 13. Since the maximum displacement occurs at a highly localized place, minor differences in the results can arise from the interpolation of synthetic strain measures (at centroids) to other places within the inverse elements. The convergence graph illustrates consistent convergence of iFEM results towards the analytical solution with the increase in inverse elements. Even with the coarse discretization of 16×16 inverse elements per side, the iFEM results are experiencing minimal deviations

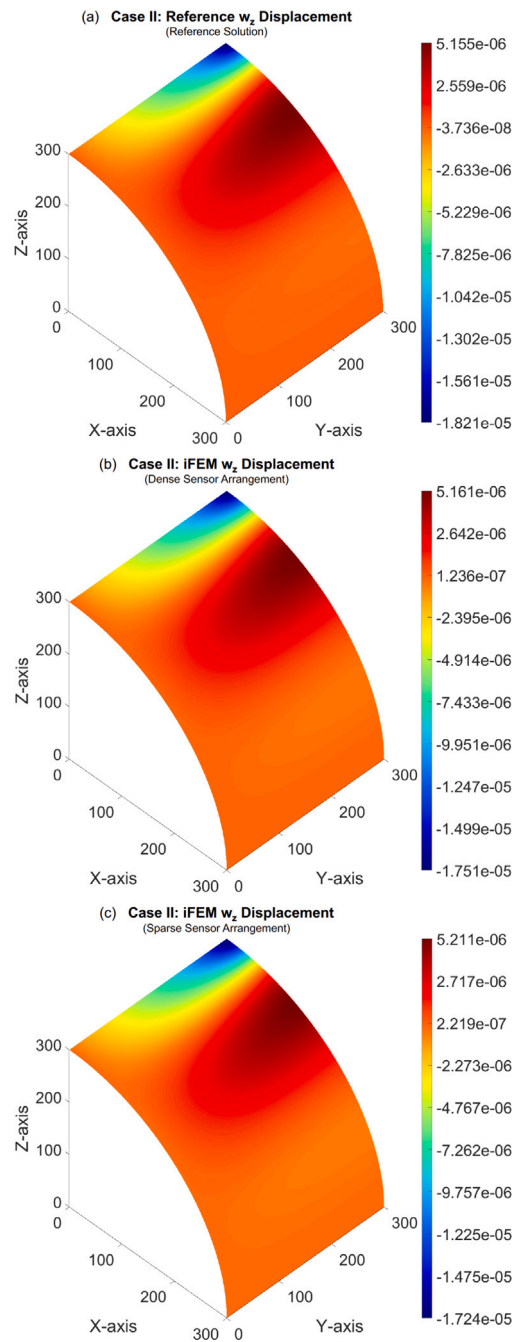


Fig. 12. Case II: Transverse displacement profiles for FEM reference solution, iFEM solution (dense-sensor), and iFEM solution (sparse-sensor).

(approximately 7% absolute error) from the reference solution. Therefore, if optimized, sensor locations and weighting functions allow for the implementation of inverse formulation with much coarser discretizations. In the subsequent numerical cases, sensor placement optimization within the inverse element domain Ω^{iel} is discussed in detail. For the given case, evaluating the iTS6 inverse element through a rigorous benchmark test for shell elements reveals its superior accuracy and robustness for shape sensing and SHM applications.

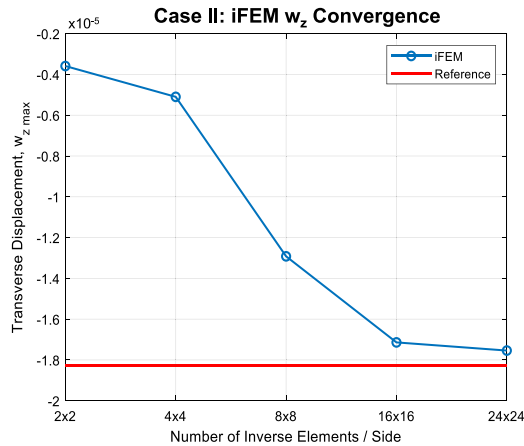


Fig. 13. Case II: iFEM convergence chart for the transverse reconstructed displacement profile.

3.2. Structures with preexisting crack

In the aerospace and naval sectors, stiff structural arrangements are used to reduce weight and enhance the overall strength-to-weight ratio of the structural assembly. Most of these engineering structures can be modeled as plate and shell structures, prone to through-thickness cracks due to fatigue and impact. Other reasons for cracks in these structures include thermal stresses, manufacturing defects, corrosion, and material degradation over time. Additionally, this section introduces a variational technique for optimizing the placement of strain sensors around the crack tip for efficient and effective iFEM analysis.

The current framework depends on accurate knowledge of crack geometry, typically obtained using Von Mises strain criteria in iFEM shape sensing applications. The proposed methodology specifically targets cracks that have the potential to grow significantly under given loading and boundary conditions, but it does not consider crack nucleation or propagation. For instance, if a crack shows an increasing risk, necessary preventive measures can be taken, e.g., reducing operational loads or scheduling maintenance to slow down or stop crack propagation. This proactive strategy effectively manages cracks before they become critical, reducing structural failure risk. The framework ensures repair effectiveness by verifying that repair schemes have successfully reduced stress concentrations. In the event of crack propagation, accurately computing SIFs becomes challenging due to changes in crack geometry. Structural assessment transitions to conventional Damage Index (DI) criteria in such cases, allowing continuous monitoring without needing immediate manual inspections. This approach ensures that structural integrity assessments remain uninterrupted while necessary model updates are scheduled for upcoming maintenance, eliminating the risk of unexpected asset downtime.

3.2.1. Cracked bar in mixed loading (Case III)

Consider a rectangular bar with a length of $l = 6$ m and a width of $w = 1$ m, having a preexisting crack of length $a = w/2$, with the crack tip located at the center of the bar, as illustrated in Fig. 14. The bottom end of the bar is fixed, while point loads $F_x = F_y = 100$ kN are applied at the top right corner along the x and y axis, respectively. As a result, the crack experiences both opening (Mode I) and sliding (Mode II) due to the mixed loading directions, necessitating the simultaneous consideration of both K_I and K_{II} stress intensity factors (SIFs) in the analysis. Isotropic material properties for the bar are $E = 210$ GPa and $\nu = 0.3$.

A high-fidelity FEM analysis is conducted using an unstructured discretization comprising 224 triangular elements, including 12 quarter-point elements at the crack tip (as shown in Fig. 14). The unstructured discretization enables the elements to adapt to complex crack surfaces without imposing stringent constraints on the element geometry. This flexibility is advantageous for implementing quarter-point elements at the crack tip. Under given in-plane loading conditions, the maximum longitudinal and lateral displacements of $u_x = 5.35$ mm and $v_y = 0.88$ mm are observed at the top left corner of the bar along x and y axis, respectively (as shown in Figs. 15 and 16). The SIFs for mixed-mode loading using the FEM displacement field are computed as $K_I = 3.16 \times 10^7$ and $K_{II} = 1.70 \times 10^6$, respectively. Synthetic strain data for subsequent iFEM analysis is generated using the displacement profiles obtained from the high-fidelity FEM model. Two iFEM scenarios are again considered for this case to evaluate the accuracy and robustness of the iTS6 inverse element in dealing with structures with preexisting cracks. In a dense sensor arrangement, strain measurements are assumed to be available for all inverse elements in the discretized geometry, as shown in Fig. 14. In contrast, in a sparse sensor arrangement, strain sensors are assumed to be placed only in the inverse elements highlighted in yellow.

First, the iFEM analysis uses a dense sensor arrangement, and the reconstructed displacement contours closely conform with the reference solution. The absolute errors observed for the maximum displacements are only 1.68% along the longitudinal axis and less than 0.1% along the lateral directions of the bar. After the displacement field reconstruction, the mixed-mode SIFs are computed using the Eqs. (53) and (54) for the full crack model. Since the synthetic strain sensors are assumed to be placed at the centroid of the inverse elements, strain interpolation to other locations may introduce interpolation errors, especially in regions with high-stress gradients, such as near crack tips. Consequently, these induced errors may lead to inaccuracies in computing SIFs via

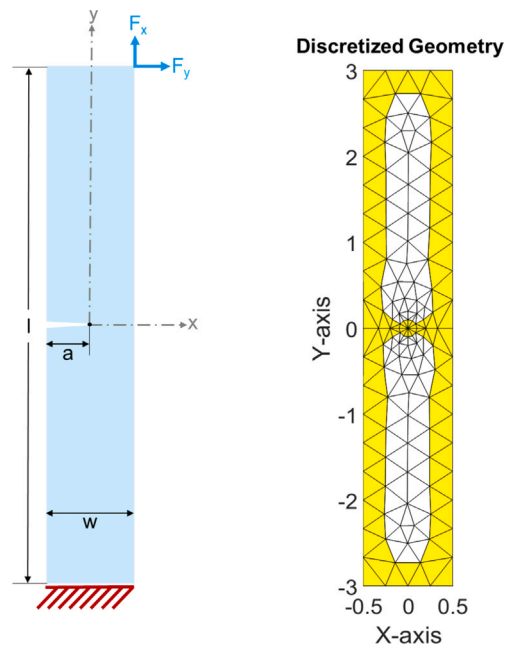


Fig. 14. Case III: Cracked rectangular bar in mixed loading and discretized geometry.

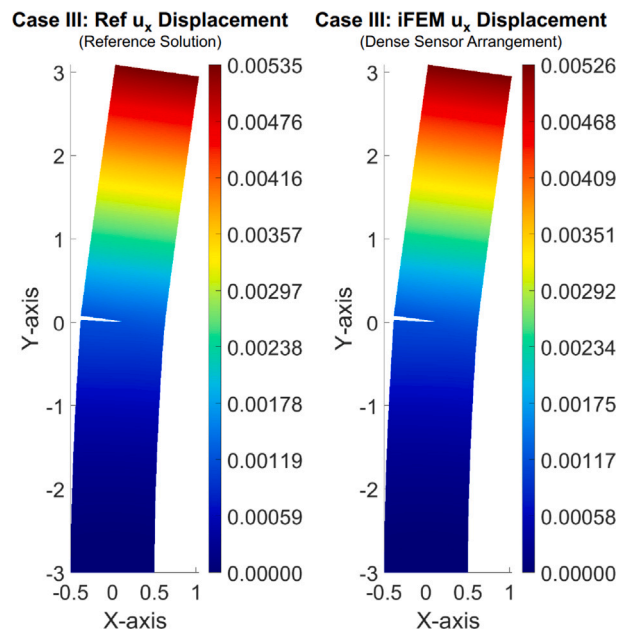


Fig. 15. Case III: Comparison of longitudinal displacement profiles between the FEM reference solution and the iFEM reconstructed solution (dense sensor).

displacement-based methods. Strain rosettes can be positioned anywhere within the inverse element domain, with common choices including Gauss point locations based on Gauss Quadrature rules for triangles and prescribed element domains, as illustrated in Fig. 17.

In a dense sensor arrangement, the variational component of the iFEM formulation is inactive, and the analysis represents an inverse problem. In such a scenario, interpolation errors can be minimized by strategically placing crack-tip sensors near the nodes (i, j, k, m, n) , which form the crack-tip displacement path for a full crack model (already shown in Fig. 7). One practical approach is to reposition sensors to Gauss location 3 using rule 6 of the numerical integration for triangles, as shown in Fig. 18. The referenced figure illustrates major Gauss locations following rule 6, and a triangular arrow at the center depicts the node numbering sequence for the inverse element vertices. Since location 3 is between nodes ij and mn on the crack-tip displacement path, it is expected

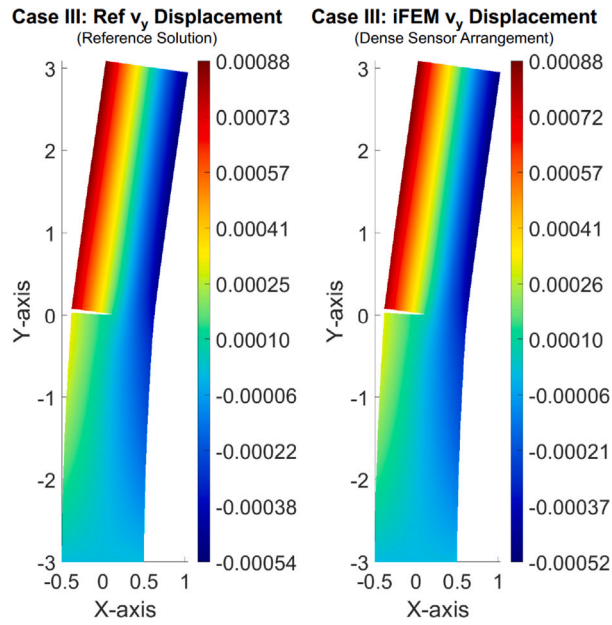


Fig. 16. Case III: Comparison of lateral displacement profiles between the FEM reference solution and the iFEM reconstructed solution (dense sensor).

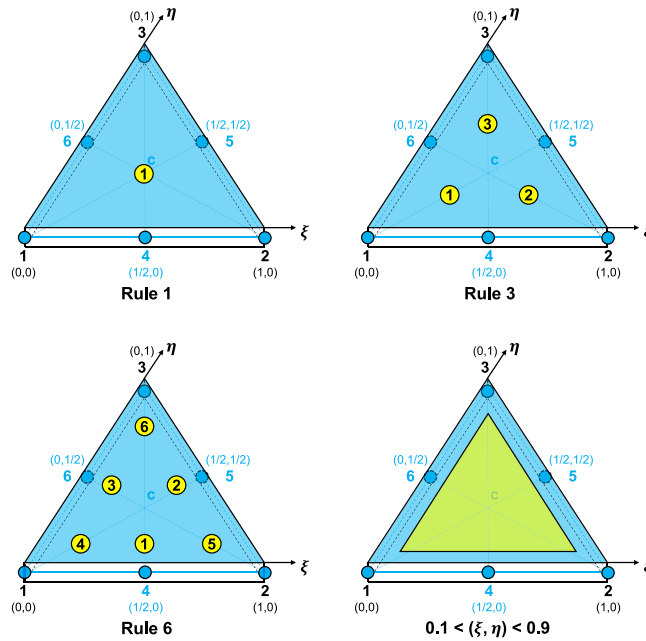


Fig. 17. Major Gauss locations in the master element for placement of sensors.

to minimize synthetic strain interpolation errors, leading to accurate computation of SIFs. Computation of SIFs at modified sensor positions (Rule 6, Gauss Location 3) under a dense sensor arrangement significantly reduces the absolute errors for the mixed-mode SIFs to 3.63% for Mode I and 1.73% for Mode II without noticeably affecting the reconstruction of displacement profiles.

On the other hand, in sparse sensor arrangements, strain sensors are placed in only a few selected inverse elements (highlighted in yellow in Fig. 14). In this scenario, the iFEM formulation is significantly influenced by the variational function; therefore, it is crucial to identify the most effective locations for strain sensors within the inverse element domains to improve shape sensing and SIF computations in the iFEM analysis. To address these challenges, this research presents a variational least squares methodology to optimize sensor locations within the inverse element domains, aiming to improve shape sensing and health assessment of engineering structures with preexisting cracks.

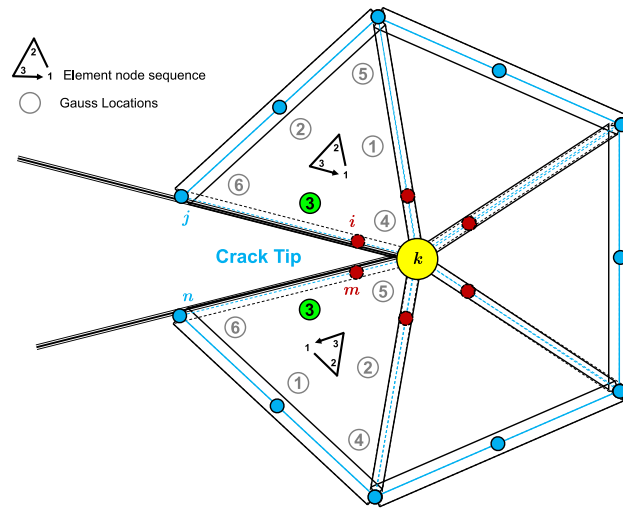


Fig. 18. Case III: Gauss location 3 following rule 6 for repositioning of the strain sensor under dense sensor arrangement.

Least Squares Effect Summary

Source	Logworth	PValue
$\xi^t_{(0.1,0.9)}$	4.865	0.00001
$\xi^t * \xi^t$	4.738	0.00002
$\xi^b_{(0.1,0.9)}$	3.644	0.00023
$\xi^b * \xi^b$	3.355	0.00044
$\xi^t * \xi^b$	2.993	0.00102
$\xi^t * \eta^b$	1.064	0.08639
$\eta^t * \eta^t$	1.051	0.08889
$\xi^b * \eta^b$	0.992	0.10183
$\eta^b_{(0.1,0.9)}$	0.819	0.1518*
$\eta^b * \eta^b$	0.706	0.19659
$\xi^t * \eta^t$	0.669	0.21427
$\eta^t_{(0.1,0.9)}$	0.613	0.2439*
$\eta^t * \xi^b$	0.050	0.89037
$\eta^t * \eta^b$	0.028	0.93677

Fig. 19. Least squares effect summary for Design of Experiments (DOE).

As discussed earlier, in the case of a sparse sensor arrangement, the location of sensors within the inverse element domain significantly influences the iFEM analysis. Therefore, simply placing the sensors at major Gauss locations is insufficient. It is essential to explore the continuous inverse elemental domain within a prescribed range of interest, i.e., $0.1 < (\xi, \eta) < 0.9$ (as depicted in Fig. 17). A custom Design of Experiments (DOE) approach is followed to generate a dataset using 25 iFEM simulations. The aim is to identify individual and interactive spatial factors that affect the output results in the iFEM analysis. The sensors above and below the crack plane are categorized into two groups, denoted by superscripts (t, b). The spatial coordinates (ξ^t, η^t) and (ξ^b, η^b) are treated as continuous input factors, while the percentage error in iFEM maximum displacements (u, v) and stress intensity factors (K_I, K_{II}) are considered as responses. Since a unique closed-form solution for optimal sensor arrangement does not exist, factors and responses can be revised according to varying optimization constraints.

The least squares effect summary in Fig. 19 reveals that the interaction terms among the input factors are effective enough to model the percentage error responses. Specifically, factors such as ξ^t and ξ^b and their interactions show significant statistical importance with high Logworth scores and low P-values, indicating their influence on the error outcomes. Also, it highlights the complexity and necessity of considering multiple interaction terms for accurate sensor placement.

Actual versus predicted errors for the maximum displacement u_{max} and v_{max} (as shown in Fig. 20) explain a high degree of correlation between the actual and predicted values, with RMSE values of 0.3738 for u_{max} and 0.6118 for v_{max} , and R-squared values over 0.99, indicating that the model explains more than 99% of the variability in error percentages. These results signify the robustness and predictive accuracy of the least squares variational technique.

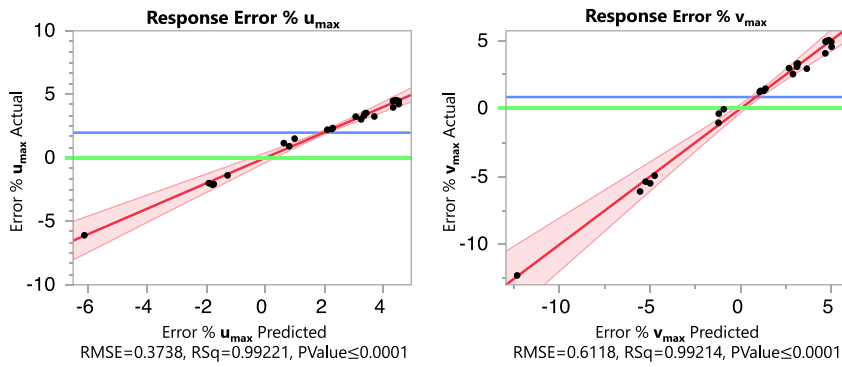


Fig. 20. Actual versus predicted percent errors for the iFEM reconstructed displacements.

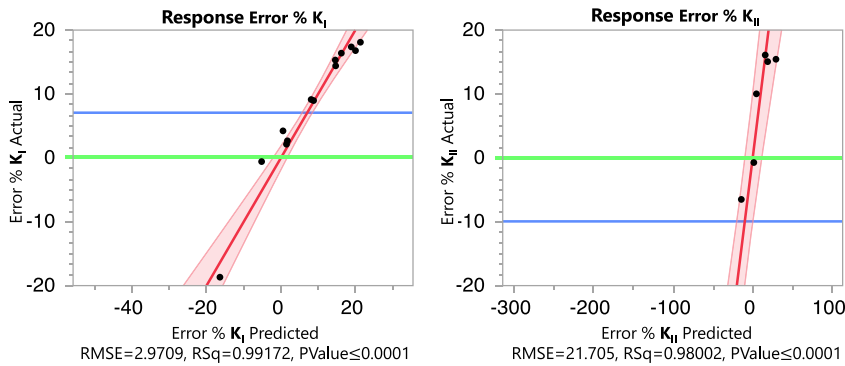


Fig. 21. Actual versus predicted percent errors for the Stress Intensity Factors (SIFs).

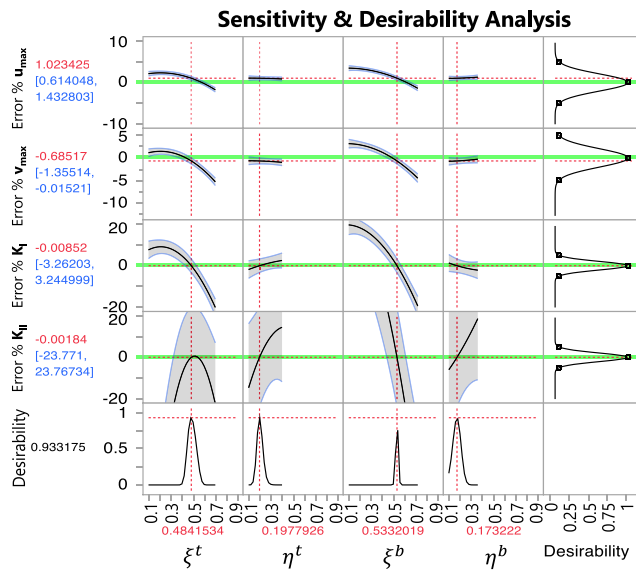


Fig. 22. Sensitivity and desirability analysis for sensor placement.

Fig. 21 shows the actual versus predicted errors for the mixed-mode SIFs. The RMSE for K_I is 2.9709, while for K_{II} it is 21.705, indicating significant variability in K_{II} as compared to K_I . Despite this, the corresponding R-squared values of 0.99172 and 0.98002 for K_I and K_{II} demonstrate the reliable predictive capabilities of the variational technique in predicting mixed-mode SIF errors.

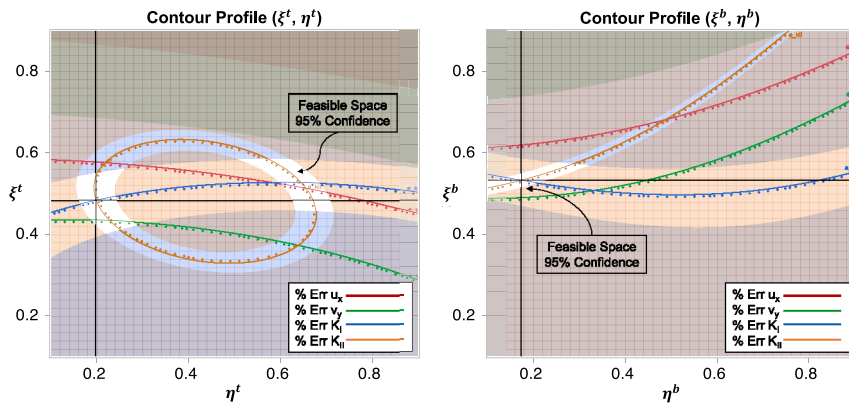


Fig. 23. Contour plots for representation of candidate solution within the inverse element domain.

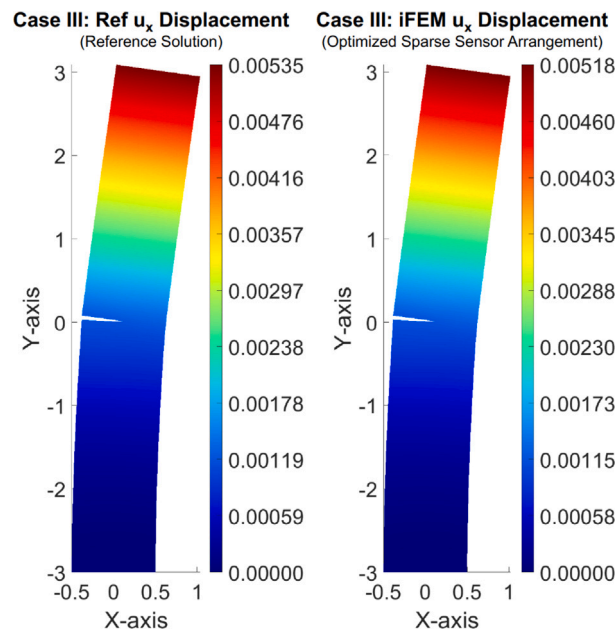


Fig. 24. Case III: Comparison of longitudinal displacement profiles between the FEM reference solution and the iFEM reconstructed solution (sparse sensor).

Sensitivity and desirability analysis is presented in Fig. 22. The sensitivity analysis interface represents the natural spatial coordinates where the placement of sensors has a significant impact on minimizing response errors for the u_{max} , v_{max} , K_I , and K_{II} . The desirability analysis illustrates the identification of a candidate solution for optimal sensor placement at $(\xi^t, \eta^t) = (0.484, 0.197)$ and $(\xi^b, \eta^b) = (0.533, 0.173)$.

The contour plots in Fig. 23 illustrate the candidate solution for two categories $^t, ^b$ of strain sensors within their respective inverse element domains. These contours also help identify active constraints influencing input factors and provide a visual guide to the regions (highlighted in white) within the respective inverse element domain where sensor placement is most effective.

The candidate solution for optimal sensor placement identified during sensitivity and desirability analysis is applied in the iFEM analysis for the sparse sensor arrangement. The reconstructed displacements (as shown in Figs. 24 and 25) are observed to be in close agreement with the FEM reference solutions, exhibiting absolute errors of only 3.17% and 2.27% along the longitudinal and lateral axes, respectively. Similarly, the computed mixed-mode SIFs closely conform to the reference values, with absolute errors of 2.43% for K_I and 7.37% for K_{II} . These results highlight the efficacy of the proposed sensor placement strategy in achieving improved accuracy displacement reconstruction and SIF computations under sparse sensor arrangements.

This study utilizes a variational approach to optimizing sensor placements to improve the accuracy of displacement reconstruction near the crack tips. The optimal sensor placement for this analysis is based on the assumed sparse sensor patterns, fixed discretization, and weighting coefficients. The successful numerical validation of Case II, which includes shape sensing and the computation of mixed-mode Stress Intensity Factors (SIFs), establishes the potential use of the iTS6 inverse element in health assessment applications

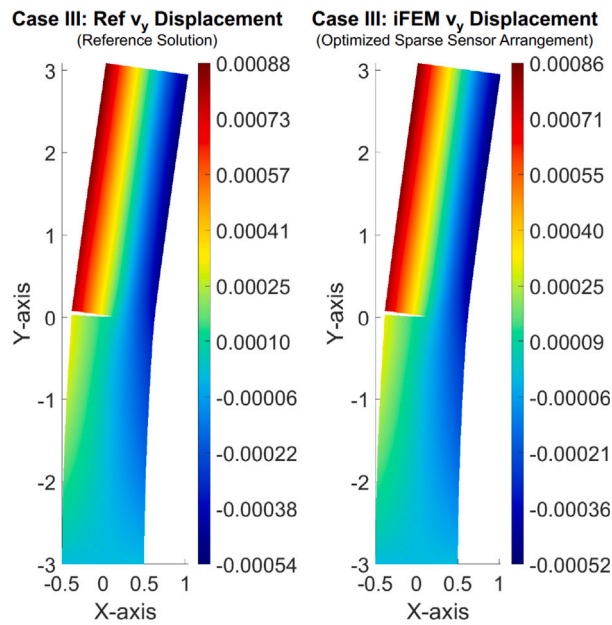


Fig. 25. Case III: Comparison of lateral displacement profiles between the FEM reference solution and the iFEM reconstructed solution (sparse sensor).

Table 2

Analysis details of Case - III.

Analysis (Type)	Sensor (Positioning)	Err u_x (Abs%)	Err v_y (Abs%)	Err K_I (Abs%)	Err K_{II} (Abs%)
iFEM	Dense (optimal)	1.68	0.10	3.63	1.73
iFEM	Sparse (optimal)	3.17	2.27	2.43	7.37
<u>Reference Solution</u>					
Analysis	Elements	u max	v max	k_I	k_{II}
FEM	224	5.35 mm	0.88 mm	3.16×10^7	1.70×10^6

for structures with preexisting cracks. Additionally, this validation confirms the efficiency of the proposed variational technique in optimizing the placement of strain sensors under sparse sensor arrangements. Table 2 summarizes the highlights of the analysis for Case III.

3.2.2. Pressurized cylinder with crack (Case-IV)

Consider an internally pressurized ($P = 1$) cylinder having a longitudinal crack with a total length of $2a = 100$, as illustrated in Fig. 26. The cylinder has a length $l = 300$, a radius $r = 300$, and a wall thickness $t = 3$. The material properties of the cylinder include Young's modulus $E = 3.0 \times 10^6$ and Poisson's ratio $\nu = 0.3$. For the given case, the crack is primarily experiencing tensile opening forces perpendicular to the crack plane, which are more likely to drive crack propagation compared to shear forces. The reference solution for the opening SIF is obtained as $K_I = 2632$ using the following empirical expression from the Cracks Handbook [51].

$$\sigma = p \frac{r}{t} \quad \text{and} \quad \lambda = \frac{a}{\sqrt{rt}}$$

$$F(\lambda) = \begin{cases} \sqrt{1 + 1.25\lambda^2} & \text{for } 0 < \lambda \leq 1 \\ 0.6 + 0.9\lambda & \text{for } 1 \leq \lambda \leq 5 \end{cases}$$

$$K_I = \sigma \sqrt{\pi a} \cdot F(\lambda)$$

$$= 2632$$

where the value $K_I = 2632$ serves as a benchmark for comparing the accuracy of SIF computations during subsequent iFEM analysis.

Initially, a high-fidelity FEM analysis is conducted employing 2308 unstructured triangular elements to model the entire cylinder. A total of 24 quarter-point elements are used to model the strain singularity in the longitudinal crack, with 12 elements placed around each crack tip. The analysis revealed the maximum longitudinal and transverse displacements of $u_x = 6.405 \times 10^{-2}$ and $w_z = 6.419 \times 10^{-2}$ at the center of the crack plane, and the maximum lateral displacements are observed at the crack tips. As

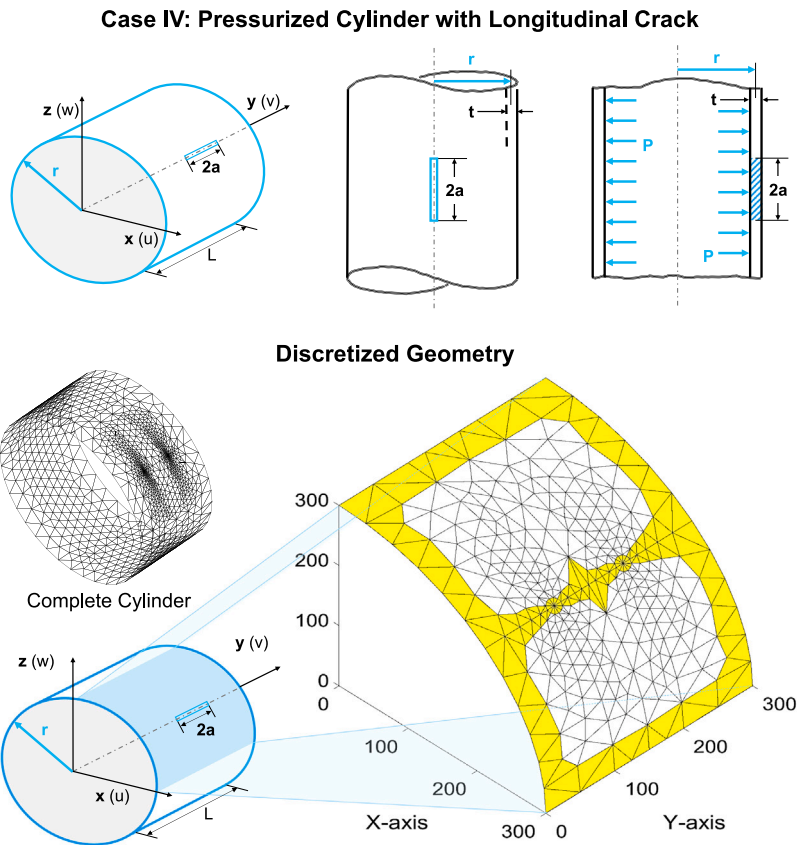


Fig. 26. Case IV: Internally pressurized cylinder with longitudinal crack and discretized geometry.

expected, the deformed displacement contours illustrated the opening of the crack faces perpendicular to the crack plane (as shown in Fig. 27a, b, and c). The SIF computed from the FEM displacement field $K_I = 2640$ is observed in close agreement with the reference SIF value of 2632. Synthetic strain data is generated using a displacement field obtained from a high-fidelity FEM model. Subsequently, two iFEM scenarios are considered for numerical validation of the iT56 inverse element: one with a dense sensor arrangement and the other with a sparse sensor arrangement. Synthetic strain measures are used for all inverse elements in the dense arrangement. In contrast, synthetic strain measures are only available to a few inverse elements highlighted in yellow (as shown in Fig. 26).

In the dense sensor arrangement, strain sensors within the crack tip inverse elements are repositioned to Gauss location 3, according to rule 6 of the numerical integration of triangles, as discussed in CASE II and illustrated in Fig. 18. The reconstructed displacement contours closely match the reference solution as shown in Fig. 27d, e, and f. The reconstructed displacement field shows an absolute error of 6.24%, 0.55%, and 5.70% in maximum longitudinal, lateral, and transverse displacements when compared against the reference solution. The opening SIF of $K_I = 2659$ is computed from the reconstructed displacements, showing an absolute error of 1.04%.

In the iFEM analysis under a sparse sensor arrangement, optimal strain sensor locations are determined using the variational technique proposed in CASE III. The candidate sensor positions are identified as $(\xi_i, \eta_i) = (0.718, 0.151)$ and $(\xi_b, \eta_b) = (0.727, 0.142)$ for the inverse elements above and below the crack plane, respectively. By repositioning strain sensors to these optimal locations, the iFEM analysis accurately reconstructs the displacement field, even with fewer sensors—less than 20% compared to a dense sensor arrangement. The reconstructed displacement profiles, shown in Fig. 27g, h, and i, exhibit slight variations when compared to the reference solutions. Since the objective function is formulated to minimize errors in the maximum displacements, the optimization process results in improved reconstruction of maximum displacements along the x , y , and z axes compared to those observed in the dense sensor arrangement. Reconstructed displacement profiles reveal absolute errors of 4.43%, 3.08%, and 0.84% in the maximum longitudinal, lateral, and transverse displacements. The SIF computed from the reconstructed displacement field closely matches the reference SIF value, with an absolute error of 2.43%. These iFEM results indicate the effectiveness of the proposed least-squares variational technique for optimal sensor placement within the inverse element domains. The same is evident from the overall reduction of errors in reconstructed displacement profiles compared to dense sensor arrangements, even with fewer strain sensors.

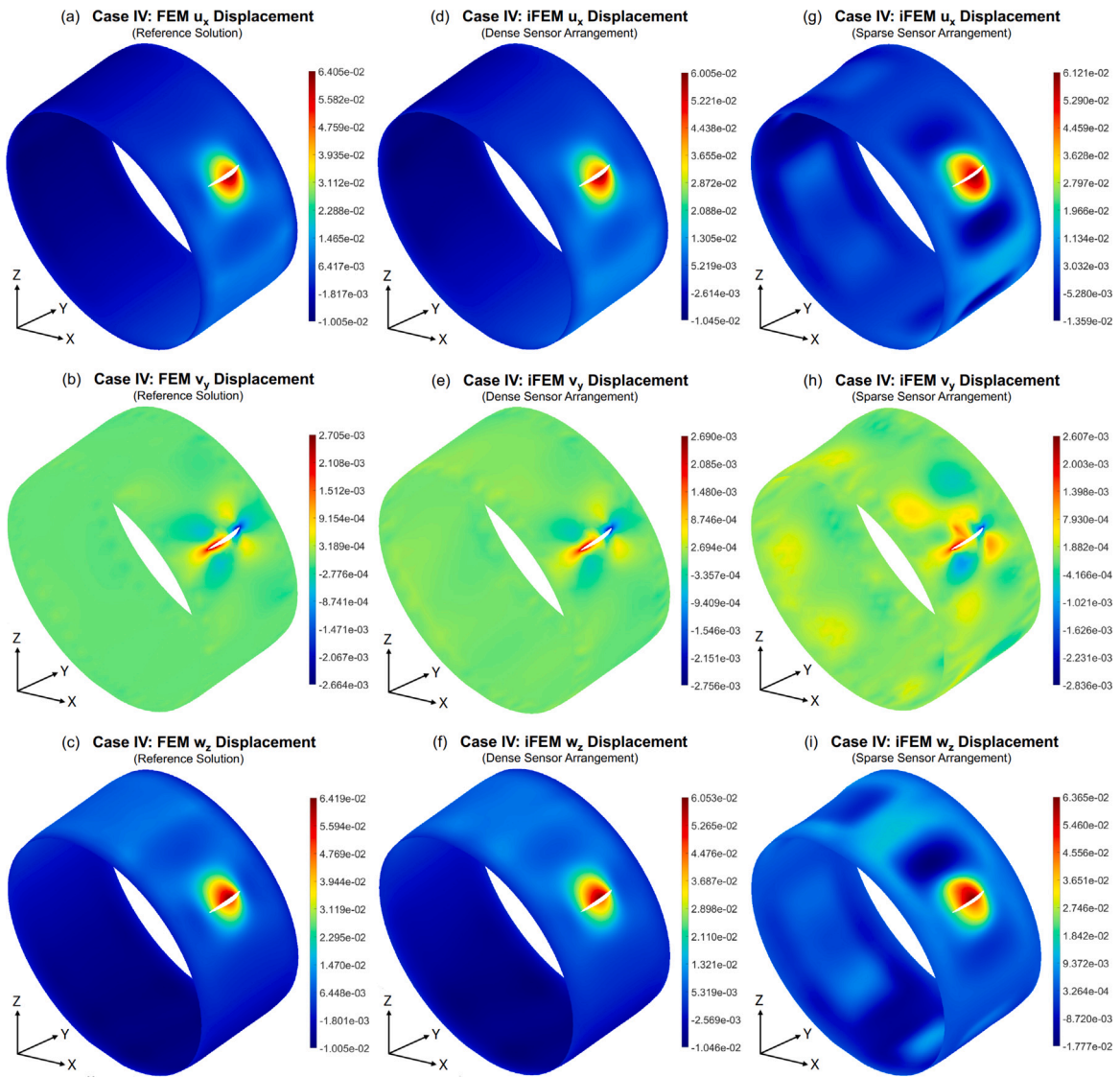


Fig. 27. Case IV: Comparison of longitudinal, lateral, and transverse displacement profiles between the FEM reference solution, iFEM reconstructed solution (dense sensor), and iFEM reconstructed solution (sparse sensor).

Table 3

Analysis details of Case - III.

Analysis (Type)	Sensor (Positioning)	Err u_x (Abs%)	Err v_y (Abs%)	Err w_z (Abs%)	Err K_I (Abs%)
iFEM	Dense (optimal)	6.24	0.55	5.70	1.04
iFEM	Sparse (optimal)	4.43	3.08	0.84	2.43
<u>Reference Solution</u>					
Analysis	Elements	u max	v max	w max	k_I
FEM	2308	0.06405	0.00270	0.06419	2640
Empirical	-	-	-	-	2632 [51]

The successful numerical validation of Case IV, which includes displacement field reconstruction and SIF computation, demonstrates the effectiveness of the iTs6 inverse element for health assessment applications of shell structures with preexisting cracks. While the proposed optimization framework addresses preexisting cracks with fixed profiles, crack propagation remains outside this analysis's scope. The optimal sensor placement for this case is based on the assumed sparse sensor pattern, fixed discretization, and weighting coefficients. A detailed sensitivity analysis considering the variability of these fixed factors can assist in further

optimizing the sensors as per application-specific configurations tailored to meet practical constraints. Table 3 further highlights the consolidated details for the given iFEM analysis.

4. Conclusion

The inverse Finite Element Method (iFEM) is a modern technique that offers full-field shape sensing, structural health monitoring (SHM), and damage assessment capabilities. Various inverse elements exist in the literature to characterize material discontinuity and degradation defects. However, the existing inverse formulations cannot analyze and accurately reconstruct crack mechanics in shell structures with preexisting cracks.

In this study, a six-node triangular inverse crack tip shell element is formulated based on the kinematics of First-Order Shear Deformation Theory (FSDT). The isoparametric inverse formulation assumes a linear shear strain field and employs a complete Gauss integration scheme for the reliable analysis of plate and shell structures. The proposed inverse element is flexible in mapping complex geometries and inherently ensures strain singularity at the crack tip by repositioning its mid-side nodes. Stress Intensity Factors (SIFs) are computed using the displacement extrapolation method based on the reconstructed displacement field.

First, the inverse shell formulation has been validated for shape sensing, considering cantilevered beam and pinched cylinder benchmark problems. After successfully validating intact structures, the inverse formulation is validated for computing stress intensity factors considering engineering structures with preexisting cracks, including a bar under in-plane loading conditions and a cylinder under internal pressurization. For dense and sparse sensor arrangements, the shape sensing profiles and stress intensity factor (SIF) are computed accurately, validating the proposed inverse formulation and successfully extending the application of iFEM in computational fracture mechanics. The proposed methodology specifically targets cracks that have the potential to grow significantly under given loading and boundary conditions, and it does not consider crack nucleation or propagation.

A proposed variational technique optimizes sensor locations within the inverse element domain to ensure accurate computation of mixed-mode stress intensity factors. The variational technique can also be utilized in general iFEM applications to optimize the placement of strain sensors within the inverse element domain. The optimal sensor placement helps reduce overall project costs when implementing structural health monitoring applications.

The proposed inverse element revealed flexibility during numerical validation in mapping complex shell geometries, such as cracks, and accurately capturing high displacement gradients near the crack tips. The framework is practically balanced between detailed crack-tip analyses using stress intensity factors (SIFs) and ongoing operational monitoring through conventional damage index (DI) methods. The proposed inverse formulation is computationally efficient and integrates seamlessly with the established iFEM framework for Structural Health Monitoring (SHM) of shell structures with preexisting cracks that pose an increased risk of propagation.

CRedit authorship contribution statement

Ihtisham Khalid: Writing – original draft, Visualization, Validation, Software, Methodology, Investigation, Data curation, Conceptualization. **Zahid Ahmed Qureshi:** Writing – review & editing, Supervision, Investigation, Conceptualization. **Yasir Ali:** Writing – review & editing, Investigation, Conceptualization. **Selda Oterkus:** Writing – review & editing, Methodology, Conceptualization. **Erkan Oterkus:** Writing – review & editing, Supervision, Methodology, Investigation, Conceptualization.

Financial disclosure

This research received no specific grant from any funding agency in the public, commercial, or non-profit sectors.

Declaration of competing interest

The authors declare that they have no known competing financial interests or personal relationships that could have appeared to influence the work reported in this paper.

Data availability

Data will be made available on request.

References

- [1] S. Hassani, U. Dackermann, A systematic review of advanced sensor technologies for non-destructive testing and structural health monitoring, *Sensors* 23 (4) (2023) 2204.
- [2] O.C. Zienkiewicz, R.L. Taylor, *The Finite Element Method Set*, Elsevier, 2005.
- [3] J. Zapomvel, I. Stachiv, P. Ferfecki, A novel method combining Monte Carlo–FEM simulations and experiments for simultaneous evaluation of the ultrathin film mass density and Young's modulus, *Mech. Syst. Signal Process.* 66 (2016) 223–231.
- [4] X. Zhou, W. He, Y. Zeng, Y. Zhang, A semi-analytical method for moving force identification of bridge structures based on the discrete cosine transform and FEM, *Mech. Syst. Signal Process.* 180 (2022) 109444.
- [5] A. Di Matteo, Dynamic response of beams excited by moving oscillators: Approximate analytical solutions for general boundary conditions, *Comput. Struct.* 280 (2023) 106989.
- [6] A.S. Bahra, P.D. Greening, Identifying axial load patterns using space frame FEMs and measured vibration data, *Mech. Syst. Signal Process.* 23 (4) (2009) 1282–1297.
- [7] Z. Yang, E. Oterkus, S. Oterkus, Peridynamic formulation for higher order functionally graded beams, *Thin-Walled Struct.* 160 (2021) 107343.
- [8] F.M.M. Rahman, S. Banerjee, Peri-elastodynamic: Peridynamic simulation method for guided waves in materials, *Mech. Syst. Signal Process.* 219 (2024) 111560.
- [9] W.L. Ko, W.L. Richards, V.T. Tran, *Displacement Theories for In-Flight Deformed Shape Predictions of Aerospace Structures*, Technical Report, NASA, 2007.
- [10] W.L. Ko, W.L. Richards, V.T. Fleischer, *Applications of Ko Displacement Theory to the Deformed Shape Predictions of the Doubly-Tapered Ikhana Wing*, Technical Report, NASA, 2009.
- [11] M. Gopinathan, G.A. Pajunen, P. Neelakanta, M. Arockaisamy, Recursive estimation of displacement and velocity in a cantilever beam using a measured set of distributed strain data, *J. Intell. Mater. Syst. Struct.* 6 (4) (1995) 537–549.
- [12] M. Manola, V. Koumoussis, Ultimate state of plane frame structures with piecewise linear yield conditions and multi-linear behavior: a reduced complementarity approach, *Comput. Struct.* 130 (2014) 22–33.
- [13] G. Foss, E. Haugse, Using modal test results to develop strain to displacement transformations, in: *Proceedings of the 13th International Modal Analysis Conference*, Vol. 2460, 1995, p. 112.
- [14] A.C. Pisoni, C. Santolini, D.E. Hauf, S. Dubowsky, Displacements in a vibrating body by strain gage measurements, in: *Proceedings-SPIE the International Society for Optical Engineering*, Citeseer, 1995, 119–119.
- [15] S. Shkarayev, R. Krashantisa, A. Tessler, An Inverse Interpolation Method Utilizing In-Flight Strain Measurements for Determining Loads and Structural Response of Aerospace Vehicles, NTRS, 2004.
- [16] J.S. Alexander Tessler, *A Variational Principle for Reconstruction of Elastic Deformations in Shear Deformable Plates and Shells*, NASA, 2003.
- [17] A. Tessler, J.L. Spangler, Inverse FEM for full-field reconstruction of elastic deformations in shear deformable plates and shells, in: *Document ID 20040086696*, NASA, 2004, pp. 1–9.
- [18] A. Kefal, E. Oterkus, A. Tessler, J.L. Spangler, A quadrilateral inverse-shell element with drilling degrees of freedom for shape sensing and structural health monitoring, *Eng. Sci. Technol. Int. J.* 19 (3) (2016) 1299–1313.
- [19] A. Kefal, An efficient curved inverse-shell element for shape sensing and structural health monitoring of cylindrical marine structures, *Ocean Eng.* 188 (2019) 106262.
- [20] I. Khalid, Z.A. Qureshi, H.A. Khan, S. Oterkus, E. Oterkus, A quadrilateral inverse plate element for real-time shape-sensing and structural health monitoring of thin plate structures, *Comput. Struct.* 305 (2024) 107551.
- [21] I. Khalid, Z.A. Qureshi, F. Siddiqui, S. Oterkus, E. Oterkus, Structural health monitoring of thin shell structures, *Int. J. Mech. Syst. Dyn.* 5 (2025) 20–39, <http://dx.doi.org/10.1002/msd2.12141>.
- [22] I. Khalid, Z.A. Qureshi, S. Oterkus, E. Oterkus, Structural health monitoring of aerospace thin plate and shell structures using the inverse finite element method (iFEM), *Thin-Walled Struct.* 209 (2025) 112923.
- [23] C. De Mooij, M. Martinez, R. Benedictus, iFEM benchmark problems for solid elements, *Smart Mater. Struct.* 28 (6) (2019) 065003.
- [24] A. Kefal, A. Tessler, E. Oterkus, An enhanced inverse finite element method for displacement and stress monitoring of multilayered composite and sandwich structures, *Compos. Struct.* 179 (2017) 514–540.
- [25] D. Poloni, D. Oboe, C. Sbarufatti, M. Giglio, Towards a stochastic inverse finite element method: a Gaussian process strain extrapolation, *Mech. Syst. Signal Process.* 189 (2023) 110056.
- [26] D. Oboe, C. Sbarufatti, M. Giglio, Physics-based strain pre-extrapolation technique for inverse Finite Element Method, *Mech. Syst. Signal Process.* 177 (2022) 109167.
- [27] F. Ganjdoust, A. Kefal, A. Tessler, A novel delamination damage detection strategy based on inverse finite element method for structural health monitoring of composite structures, *Mech. Syst. Signal Process.* 192 (2023) 110202.
- [28] L. Colombo, D. Oboe, C. Sbarufatti, F. Cadini, S. Russo, M. Giglio, Shape sensing and damage identification with iFEM on a composite structure subjected to impact damage and non-trivial boundary conditions, *Mech. Syst. Signal Process.* 148 (2021) 107163.
- [29] M. Li, D. Jia, Z. Wu, S. Qiu, W. He, Structural damage identification using strain mode differences by the iFEM based on the convolutional neural network (CNN), *Mech. Syst. Signal Process.* 165 (2022) 108289.
- [30] L. Colombo, C. Sbarufatti, M. Giglio, Definition of a load adaptive baseline by inverse finite element method for structural damage identification, *Mech. Syst. Signal Process.* 120 (2019) 584–607.
- [31] F. Dipietrangolo, F. Nicassio, G. Scarselli, Structural Health Monitoring for impact localisation via machine learning, *Mech. Syst. Signal Process.* 183 (2023) 109621.
- [32] D. Sen, A. Aghazadeh, A. Mousavi, S. Nagarajaiah, R. Baraniuk, A. Dabak, Data-driven semi-supervised and supervised learning algorithms for health monitoring of pipes, *Mech. Syst. Signal Process.* 131 (2019) 524–537.
- [33] E. Samaniego, C. Anitescu, S. Goswami, V.M. Nguyen-Thanh, H. Guo, K. Hamdia, X. Zhuang, T. Rabczuk, An energy approach to the solution of partial differential equations in computational mechanics via machine learning: Concepts, implementation and applications, *Comput. Methods Appl. Mech. Engrg.* 362 (2020) 112790.
- [34] B. Wang, Z. Li, Z. Xu, Z. Sun, K. Tian, Digital twin modeling for structural strength monitoring via transfer learning-based multi-source data fusion, *Mech. Syst. Signal Process.* 200 (2023) 110625.
- [35] L. Bull, T. Rogers, C. Wickramarachchi, E. Cross, K. Worden, N. Dervilis, Probabilistic active learning: an online framework for structural health monitoring, *Mech. Syst. Signal Process.* 134 (2019) 106294.
- [36] J.-Y. Wu, V.P. Nguyen, C.T. Nguyen, D. Sutula, S. Sinaie, S.P. Bordas, Phase-field modeling of fracture, *Adv. Appl. Mech.* 53 (2020) 1–183.
- [37] N. Noii, M. Fan, T. Wick, Y. Jin, A quasi-monolithic phase-field description for orthotropic anisotropic fracture with adaptive mesh refinement and primal-dual active set method, *Eng. Fract. Mech.* 258 (2021) 108060.
- [38] N. Noii, D. Milijasevic, H. Waisman, A. Khodadadian, Fatigue failure theory for lithium diffusion induced fracture in lithium-ion battery electrode particles, *Comput. Methods Appl. Mech. Engrg.* 428 (2024) 117068.

- [39] D. Proserpio, M. Ambati, L. De Lorenzis, J. Kiendl, Phase-field simulation of ductile fracture in shell structures, *Comput. Methods Appl. Mech. Engrg.* 385 (2021) 114019.
- [40] J. Kiendl, M. Ambati, L. De Lorenzis, H. Gomez, A. Reali, Phase-field description of brittle fracture in plates and shells, *Comput. Methods Appl. Mech. Engrg.* 312 (2016) 374–394.
- [41] N. Nohi, A. Khodadadian, T. Wick, Bayesian inversion using global-local forward models applied to fracture propagation in porous media, *Int. J. Multiscale Comput. Eng.* 20 (3) (2022).
- [42] O. Zienkiewicz, R. Taylor, P. Papadopoulos, E. Onate, Plate bending elements with discrete constraints: new triangular elements, *Comput. Struct.* 35 (4) (1990) 505–522.
- [43] T.J.R. Hughes, T.E. Tezduyar, Finite elements based upon mindlin plate theory with particular reference to the four-node bilinear isoparametric element, *J. Appl. Mech.* 48 (3) (1981) 587–596.
- [44] E. Onate, R. Taylor, O. Zienkiewicz, Consistent formulation of shear constrained Reissner-Mindlin plate elements, in: *Discretization Methods in Structural Mechanics: IUTAM/IACM Symposium Vienna/Austria, 5.–9.6. 1989*, Springer, 1990, pp. 169–180.
- [45] O. Eugenio, *Structural Analysis with the Finite Element Method: Linear Statics*, Springer Netherlands, 2009.
- [46] R.S. Barsoum, Triangular quarter-point elements as elastic and perfectly-plastic crack tip elements, *Internat. J. Numer. Methods Engrg.* 11 (1) (1977) 85–98.
- [47] E. Oñate, *Structural Analysis with the Finite Element Method. Linear Statics: Volume 2: Beams, Plates and Shells*, Springer Science & Business Media, 2013.
- [48] N. Zhu, E. Oterkus, Calculation of stress intensity factor using displacement extrapolation method in peridynamic framework, *J. Mech.* 36 (2) (2020) 235–243.
- [49] S. Timoshenko, J. Goodier, *Theory of elasticity*, Inc. N. Y. 1 (1951) 35–39.
- [50] T. Belytschko, H. Stolarski, W.K. Liu, N. Carpenter, J.S. Ong, Stress projection for membrane and shear locking in shell finite elements, *Comput. Methods Appl. Mech. Engrg.* 51 (1–3) (1985) 221–258.
- [51] H. Tada, P. Paris, G. Irwin, *The Stress Analysis of Cracks Handbook*, ASME Press, 2000.